5 # Quasi 12 h inertia-gravity waves in the lower

6 # mesosphere observed by the PANSY radar at Syowa

7 # Station (39.6°E, 69.0°S)

11 Ryosuke Shibuya[1], Kaoru Sato[1], Masaki Tsutsumi[2,3],

12 Toru Sato[4], Yoshihiro Tomikawa[2,3],

13 Koji Nishimura[2,3] and Masashi Kohma[1]

15 [1] *Department of Earth and Planetary Science, The University of Tokyo, Tokyo, Japan*

16 [2] *National Institute of Polar Research, Tachikawa, Japan*

17 [3] *The Graduate University for Advanced Studies (SOKENDAI), Tokyo, Japan*

18 [4] *Department of Communications and Computer Engineering, Kyoto University, Japan*

20 *Corresponding to,* Ryosuke Shibuya, The University of Tokyo, 7-3-1 Hongo, Bunkyo-ku,

21 Tokyo 113-0033, Japan. E-mail: shibuya@eps.s.u-tokyo.ac.jp.

1 **Abstract**

2 The first observations made by a complete PANSY radar system (Program of the Antarctic

3 Syowa MST/IS Radar) installed at Syowa Station (39.6°E, 69.0°S) were successfully

4 performed from March 16 – 24, 2015. Over this period, quasi-half-day period (12 h)

5 disturbances in the lower mesosphere at heights of 70 km to 80 km were observed. Estimated

6 vertical wavelengths, wave periods and vertical phase velocities of the disturbances were

7 approximately 13.7 km, 12.3 h and -0.3 m s^{-1}, respectively. Under the working hypothesis that

8 such disturbances are attributable to inertia-gravity waves, wave parameters are estimated

9 using a hodograph analysis. The estimated horizontal wavelengths are longer than 1100 km,

10 and the wavenumber vectors tend to point northeastward or southwestward. Using the non-

11 hydrostatic numerical model with a model top of 87 km, quasi 12 h disturbances in the

12 mesosphere were successfully simulated. We show that quasi 12 h disturbances are due to

13 wave-like disturbances with horizontal wavelengths longer than 1400 km and are not due to

14 semi-diurnal migrating tides. Wave parameters, such as horizontal wavelengths, vertical

15 wavelengths and wave periods, simulated by the model agree well with those estimated by the

16 PANSY radar observations under the above-mentioned assumption. The parameters of the

17 simulated waves are consistent with the dispersion relationship of the inertia-gravity wave.

18 These results indicate that the quasi 12 h disturbances observed by the PANSY radar are

19 attributable to large-scale inertia-gravity waves. By examining a residual of the nonlinear

20 balance equation, it is inferred that the inertia-gravity waves are likely generated by the

21 spontaneous radiation mechanism of two different jet streams. One is the mid-latitude

22 tropospheric jet around the tropopause while the other is the polar night jet. Large vertical

23 fluxes of zonal and meridional momentum associated with large-scale inertia-gravity waves

24 are distributed across a slanted region from the mid-latitude lower stratosphere to the polar

25 mesosphere in the meridional cross-section. Moreover, the vertical flux of the zonal momentum

26 has a strong negative peak in the mesosphere, suggesting that some large-scale inertia-gravity

1 waves originate in the upper stratosphere. [335words]

3 Keywords: Gravity wave, polar region, mesosphere, the PANSY radar

5 **1. Introduction**

6 Gravity waves are atmospheric waves with a restoring force of buoyancy that can transport

7 momentum upward from the troposphere to the middle atmosphere (e.g., Fritts and Alexander

8 2003). Momentum deposition by gravity waves in the mesosphere is a major driving force for

9 the summer to winter pole material circulation in the mesosphere (e.g., Plumb 2002). Adiabatic

10 heating/cooling associated with vertical flow branches of the circulation maintain the thermal

11 structure, which is considerably different from the radiative equilibrium state. Gravity waves

12 also play an essential role in driving the quasi-biennial oscillation (QBO) and semi-annual

13 oscillation in the equatorial stratosphere (Sato and Dunkerton 1997; Haynes 1998; Baldwin et

14 al., 2003). In addition, it has been shown that gravity wave forcing is essential to the summer

15 hemispheric low-latitude part of winter stratospheric circulation (Okamoto et al., 2011).

16 Many observational studies have closely examined characteristics of gravity waves in the

17 troposphere, stratosphere and mesosphere (e.g., Sato 1994; Sato and Yamada, 1994; Pavelin et

18 al., 2001; Lane et al., 2004; Nastrom and Eaton 2006; Vaughan and Worthington, 2007;

19 Nakamura et al., 1993; Li et al., 2007; Lu et al., 2009; Nicolls et al., 2010; Chen et al., 2013).

20 It is well known that gravity waves have wide spectral ranges of horizontal wavelength from

21 several kilometers to several thousand kilometers and of observed period from several minutes

22 to several hours. Recently, several numerical models directly resolve large parts of gravity

23 wave spectra (the KANTO model, Watanabe et al., 2008; WACCM, Liu et al., 2014; KMCM,

24 Becker, 2009). However, due to their short horizontal wavelengths, many climate models

25 utilize parameterization methods to calculate momentum deposition by unresolved gravity

26 waves (e.g., McFarlane 1987; Scinocca 2003; Richter et al., 2009). As parameterization

1   methods involve several tuning parameters related to characteristics of gravity waves,

2   observational constraints on tuning parameters are inevitably required (e.g., Alexander et al.

3   2010).

4   Geller et al. (2013) showed that parameterized gravity waves in climate models are not

5   realistic in several aspects in comparison to high-resolution observational data (satellites,

6   isopycnic balloon observations and radiosondes) and gravity wave permitting general

7   circulation models. In particular, they showed that gravity wave sources in the parameterization

8   can be poorly specified in high latitude regions. Such an improper specification of gravity wave

9   sources in southern high latitude regions is considered to lead several serious problems. One

10   of these problems is the so-called cold-pole bias, which most climate models present in the

11   polar winter stratosphere (Eyring et al., 2010; McLandress et al. 2012). This bias is closely

12   related to significant delays in the breakdown of the stratospheric polar vortex in the Antarctic

13   (Stolarski et al., 2006). Gravity waves in the southern polar region modify formations of polar

14   stratospheric clouds (PSCs), which can enhance ozone depletion in the polar lower stratosphere

15   (Shibata et al., 2003; Watanabe et al. 2006; McDonald et al., 2009; Kohma and Sato, 2011).

16   Moreover, Chu et al. (2011) reported that inertia-gravity waves in the polar mesosphere also

17   affect the formation of polar mesospheric clouds (PMCs). Thus, observational studies of

18   gravity waves around the southern high latitude region are quite important (e.g., Hertzog et al.,

19   2008).

20   Recently, a Mesosphere-Stratosphere-Troposphere (MST) radar (or VHF clear-air

21   Doppler radar) system was installed in the Antarctic. The system has completed continuous

22   observations since April 30, 2012 at Syowa Station (69.0°S, 39.6°E) (the PANSY radar; Sato

23   et al., 2014). The radar system provides vertical profiles of three-dimensional winds at high

24   time and height resolutions. The PANSY radar system is a powerful tool for examining gravity

25   waves in the high latitude region and many other scientific issues related to the polar

1   atmosphere.

2   One interesting phenomenon observed in the polar mesosphere is a large-amplitude wave-

3   like disturbance with near inertia-frequency (approximately 12 h) that many previous studies

4   have examined (e.g., Murphy et al., 2006; Akmaev et al., 2016). There are several explanations

5   for the existence of such oscillations; Fraser and Khan (1990) and Fisher et al. (2002) posited

6   that these oscillations are attributable to a semi-diurnal migrating tide. Waterscheid et al. (1986)

7   and Collins et al. (1992) attributed these oscillations to a "pseudo-tide" mechanism related to

8   gravity-wave momentum deposition modulated by a semi-diurnal migrating tide. Hagan and

9   Forbes (2003) investigated the atmospheric response to forcing by zonally asymmetric latent

10   heat release in the troposphere. Talaat and Mayr (2011) found that internal oscillations may be

11   caused by parameterized gravity waves in the model. Other studies (Hernandez et al., 1993;

12   Forbes et al., 1995, 1999; Fritts et al, 1998; Portnyagin et al. 1998; Yamashita et al., 2002; Wu

13   et al., 2003, Aso 2007, Murphy et al., 2009) suggest that these oscillations are due to semi-

14   diurnal non-migrating tides with zonal wavenumber $s = 1$ generated by nonlinear interactions

15   between $s = 1$ stationary planetary waves and semi-diurnal migrating tides. Mayr et al. (2005a,

16   b) emphasized the importance of gravity wave filtering effects on nonlinear interactions. Riggin

17   et al. (1999) showed that the zonal wavenumber of the 12 h wave is close to two in the winter

18   and is one in the summer based on radar observations conducted at McMurdo (77.8ºS) and

19   Halley (75.8ºS). Wu et al. (2002) suggested that $s = 1$ semi-diurnal non-migrating tides are

20   significant at latitudes of higher than 78° and that a mixture of semi-diurnal migrating tides and

21   $s = 1$ semi-diurnal non-migrating tides appears at between 68° and 78°.

22   The first successful observation with a complete system of the PANSY radar was

23   performed for March 16 – 24, 2015. In this study, we used this observational dataset. During

24   this observation period, strong wave-like disturbances with a wave period of about 12 h were

25   found in the lower mesosphere. Using PANSY radar data and a gravity wave resolving model,

1   generation and propagation mechanisms of such disturbances were examined. It is suggested

2   that wave-like disturbances with a wave period of about 12 h are attributable to large-scale

3   inertia-gravity waves with horizontal wavelengths of larger than 1100 km.

4   The present article is organized as follows. The methodology used is described in Section

5   2. Observational results are presented in Section 3. The results of the model simulations are

6   given and compared with radar observations in Section 4. Propagation characteristics and the

7   wave generation mechanism are also examined. A discussion is presented in Section 5, and

8   Section 6 summarizes the results and provides concluding remarks.

2.   Methodology

2.1. The PANSY radar observations

12   The PANSY (Program of the Antarctic Syowa MST/IS radar) radar system is the first

13   MST/IS radar system installed at Syowa Station (39.6°E, 69.0°S) for observing the Antarctic

14   atmosphere within a height range of 1.5–500 km. The PANSY radar system is a pulse-

15   modulated monostatic Doppler radar system with an active phased array system mechanism

16   consisting of 1045 crossed-Yagi antennas. The PANSY radar system is designed to observe

17   three-dimensional winds at a high time resolution and vertical resolution along beam directions

18   of Δt = ~1 min and Δz = 150 m in the troposphere and lower stratosphere, respectively, and

19   of Δz = 600 m in the mesosphere. The accuracy of line-of-sight wind velocity is about 0.1 m

20   s^{-1}. As the target of MST radar is atmospheric turbulence, wind measurements can be made

21   under all weather conditions. Continuous observations have been made by the PANSY radar

22   through a partial system since April 30, 2012. The first observation with a complete system of

23   the PANSY radar observation was successfully performed for March 16 – 24, 2015. See Sato

24   et al. (2014) for further information on the PANSY radar system and for a list of future studies

25   to be conducted based on this system. For the March 16 – 24, 2015 period, strong polar

26   mesosphere winter echoes, which likely resulted from the largest magnetic storm event

1 occurring during the solar cycle 24 (Kataoka et al., 2015), were observed by the PANSY radar

2 system.

3 The PANSY radar data that we used are line-of-sight wind velocities of five vertical beams

4 tilted east, west, north and south at a zenith angle of θ =10°. Vertical wind components are

5 directly estimated from the vertical beam. Zonal (meridional) wind components are obtained

6 using a pair of line-of-sight velocities of the east and west beams (the north and south beams).

7 For example, line-of-sight velocities of the east and west beams, $V_{\pm\theta}$, are composed of zonal

8 and vertical components of the wind velocity vectors $(u_{\pm\theta}, w_{\pm\theta})$ in the targeted volume

9 ranges:

$$V_{\pm\theta} = \pm u_{\pm\theta} \sin\theta + w_{\pm\theta} \cos\theta.$$

10 By assuming that the wind field is homogeneous at each height, i.e., $u_{+\theta} = u_{-\theta} \equiv u$ and

11 $w_{+\theta} = w_{-\theta} \equiv w$, we can estimate zonal wind components as:

$$u = \frac{V_{+\theta} - V_{-\theta}}{2\sin\theta}.$$

12 The vertical flux of zonal momentum is directly estimated from variances of line-of-sight wind

13 fluctuations (Vincent and Reid, 1983):

$$\overline{V'^2_{\pm\theta}} = \overline{u'^2_{\pm\theta}} \sin^2\theta + \overline{w'^2_{\pm\theta}} \cos^2\theta \pm \overline{u'_{\pm\theta}w'_{\pm\theta}} \sin 2\theta$$

14 By assuming that the flux and variance fields are homogeneous ($\overline{u'^2_{+\theta}} = \overline{u'^2_{-\theta}} \equiv \overline{u'^2}$, $\overline{w'^2_{+\theta}} =$

15 $\overline{w'^2_{-\theta}} \equiv \overline{w'^2}$ and $\overline{u'_{+\theta}w'_{+\theta}} = \overline{u'_{-\theta}w'_{-\theta}} \equiv \overline{u'w'}$), we obtain:

$$\overline{u'w'} = \frac{\overline{V'^2_{+\theta}} - \overline{V'^2_{-\theta}}}{2\sin 2\theta}.$$

20 This assumption is less strict than that used for the u and w estimates. Thus, the method based

21 on MST radars provides quite accurate estimates of momentum fluxes. The meridional wind

22 component and the vertical flux of meridional momentum can be estimated in a similar manner.

24 **2.2. Numerical setup for non-hydrostatic model simulation**

25 The simulation was performed using the Non-hydrostatic Icosahedral Atmospheric Model

1   (NICAM), which a global cloud resolving model (Satoh et al., 2008, Satoh et al., 2014). A non-

2   hydrostatic dynamical core of the NICAM was developed from icosahedral grids modified by

3   the spring dynamics method (Tomita et al., 2002). The NICAM is unique in its use of a flux-

4   form non-hydrostatic equation system that assures the conservation of total mass, momentum

5   and energy over the domain.

2.2.1. Horizontal and vertical coordinate system

8   Resolutions of horizontal icosahedral grids are represented by glevel-n (grid division level

9   n). Glevel-0 denotes the original icosahedron. By dividing each triangle into four small

10   triangles recursively, one-higher resolution is obtained. The total number of grid points is $N_g =$

11    $10 \cdot 4^n + 2$ for glevel-n. The actual resolution corresponds to the square root of the averaged

12   control volume area, $\Delta x \equiv \sqrt{4\pi R_E^2/N_g}$, where R_E is the Earth's radius. A glevel-7 grid is

13   used in this study ($\Delta x \sim$ 28 km).

14   Recently, Shibuya et al. (2016) developed a new grid configuration for quasi-uniform and

15   regionally fine meshes within a circular region with icosahedral grids using spring dynamics.

16   This method clusters grid points over the sphere into the circular region (the targeted region)

17   and realizes finer meshes than original icosahedral grids. By introducing sets of mathematical

18   constraints, it has been shown that the minimum resolution within the targeted region is

19   uniquely determined by the area of the targeted region alone. In this study, the targeted region

20   for a given glevel is a region south of 30°S centered at the South Pole. Figure 1a shows an

21   illustration of the stretched grid which is roughened up to glevel-3. Figure 1b shows a

22   horizontal map of a normalized grid interval defined as $d(\lambda, \phi)/\Delta x$, where d denotes grid

23   intervals as a function of the longitude, λ, and the latitude, ϕ. In this case, the horizontal

24   resolution in the targeted region is roughly 18 km.

25   To simulate structures of disturbances from the stratosphere to the mesosphere, the vertical

1   grid spacing is 400 m at heights from 2.4 km to 80 km. It should be noted that according to

2   Watanabe et al. (2015), gravity wave momentum flux is not heavily dependent on model

3   vertical spacing in the middle atmosphere when $\Delta z < 400$ m. The number of vertical grids is

4   217. To prevent unphysical waves reflection at the top of the boundary, a 7 km thick sponge

5   layer is set above z = 80 km. The second-order Laplacian horizontal hyper-viscosity diffusion

6   and Rayleigh damping for the vertical velocity are used for the sponge layer. An *e*-folding time

7   of the ∇^2 horizontal diffusion for the $2\Delta x$ wave at the top of the model is 4 s, and an *e*-folding

8   time of the Rayleigh damping for the vertical velocity for the top of the model is 216 s. The

9   diffusivity level gradually increases from the bottom to the top of the sponge layer. We confirm

10   that little wave reflection near the sponge layer occurs under this setting (not shown).

12   **2.2.2. Initial condition and other physical schemes**

13   MERRA reanalysis data based on the Goddard Earth Observing System Data Analysis

14   System, Version 5 (GEOS-5 DAS; Rienecker et al. 2011) is used as the initial condition. In the

15   MERRA reanalysis data, the following two types of 3-D fields are provided: one set is produced

16   through the corrector segment of the Incremental Analysis Update (IAU, Bloom et al., 1996)

17   cycle ($1.25° \times 1.25°$ and 42 vertical levels whose top is 0.1 hPa) and the other pertains to fields

18   resulting from Gridpoint Statistical Interpolation analyses (GSI analysis, e.g., Wu et al., 2002)

19   on the native horizontal grid and on native model vertical levels ($0.75° \times 0.75°$ and 72 vertical

20   levels whose top is 0.01 hPa). We use the former 3-D assimilated fields for 1000 hPa to 0.1 hPa

21   and the latter 3-D analyzed fields for 0.1 hPa to 0.01 hPa for the initial condition of the NICAM

22   simulation to prepare realistic atmospheric fields in the mesosphere for 0000 UTC on March

23   17, 2015. The latter 3-D analyzed fields were only used at above 0.1 hPa, as variables of vertical

24   pressure velocity, cloud liquid water and ice mixing ratios are not included. Vertical pressure

25   velocities, cloud liquid water and ice mixing ratios above 0.1 hPa are set to zero. A time

26   integration was performed until 0000 UTC on March 24. The time step was 15 seconds. As

1   part of the boundary layer scheme, MYNN level 2 (Nakanishi and Niino, 2004) was used. No

2   cumulous or gravity wave parameterization was employed. The model output was recorded

3   every 1 hour. It should be noted that this model does not use the nudging method as an external

4   forcing for the atmospheric component.

6   **3. Observational results**

7   Figure 2a shows the time-height section of the line-of-sight wind velocity observed by the

8   east beam of the PANSY radar system. In the lower stratosphere, wavy structures with short

9   vertical wavelengths are shown. Shibuya et al. (2015) showed that such a structure observed in

10   May of 2013 at Syowa Station was due to inertia-gravity waves with a vertical wavelength of

11   about 2 km. In the mesosphere, strong echoes were detected at heights of 60 km to 80 km over

12   this time period. These are likely polar mesosphere winter echoes (PMWEs) associated with

13   increased ionization during the solar flare event occurring on March 17, 2015 (Kataoka et al.

14   2015). As is shown in Figure 2a, strong wave-like disturbances were observed in the

15   mesosphere. Figures 2b and 2c, respectively show line-of-sight wind velocities of the east and

16   west beams at heights of 65 - 80 km for 00 UTC on March 21 to 00 UTC on March 24. In

17   Figures 2b and 2c, it is clear that phases of dominant disturbances propagate downward; a

18   vertical phase velocity (broken line) and an observed period (a green arrow) are about −0.3 m

19   s^{-1} and 12.3 h, respectively. This indicates that the vertical wavelength is about 13.8 km.

20   As the zenith angle of tilted beams of the PANSY radar system is θ =10°, locations of

21   the observation points by opposite beams in the mesosphere are separated by approximately 25

22   km at a height of 70 km. Figures 3a and 3b show time-height sections of estimated zonal and

23   meridional wind components.

24   Based on the working hypothesis that wind disturbances in the mesosphere are due to

25   inertia-gravity waves, wave parameters are estimated using a hodograph analysis. A hodograph

26   analysis (e.g., Hirota and Niki 1986; Sato 1994) is applied to wind fluctuations at heights of

1 73.2 km, 73.8 km and 74.4 km for March 22 and at the heights of 70.8 km, 71.4 km and 72.0

2 km for March 23. In this analysis, hodographs are made in the time direction.

3   First, wave zonal (u') and meridional (v') wind fluctuations were fitted to sinusoidal

4 functions as follows:

$$u' = \hat{u}\sin(\omega t + \theta_u) + u_{\mathrm{o}}$$
$$v' = \hat{v}\sin(\omega t + \theta_v) + v_{\mathrm{o}},$$

(1)

5 where $\hat{u}$ and $\hat{v}$ are the amplitudes of u' and v', respectively, ω is the observed wave

6 frequency, t is time, θ_u and θ_v are phases of zonal and meridional wind fluctuations, and u_{o}

7 and v_{o} are offsets of zonal and meridional wind fluctuations, respectively. Parameters ($\hat{u}$, $\hat{v}$,

8 ω, θ_u, θ_v, u_{o} and v_{o}) are determined using a nonlinear least square method. Figure 4 shows

9 a time series of observed horizontal wind fluctuations and results of the fitting at 70.8 km and

10 72.0 km for March 23. It is clear that the observed wind fluctuations seem to have a sinusoidal

11 form with a period of about 12 h, and the fitting is successful. Moreover, phases of zonal and

12 meridional wind fluctuations at 72.0 km seem to be advanced compared to those at 70.8 km.

13 Using these phase differences in zonal and meridional wind fluctuations, vertical wavenumbers

14 for zonal and meridional fluctuations are estimated, respectively. Table 1a summarizes

15 parameters such as wave frequencies, vertical wavenumbers and vertical phase velocities

16 estimated from u' and v'. The estimated period ranges from 11.0 h to 13.8 h, which is quasi

17 12 h. The estimated vertical wavelengths are 12.0 km and 8.5 km for u' and v' for March 22

18 and are 15.4 km and 12.3 km for u' and v' for March 23, respectively. Thus, the vertical

19 phase velocities are −0.26 m s^{-1} and −0.19 m s^{-1} for u' and v' for March 22 and −0.35 m s^{-1}

20 and −0.28 m s^{-1} for u' and v' for March 23, respectively. Although the estimation based on

21 v' for March 22 shows slightly different values, the vertical phase velocities and observed

22 periods agree well with the rough estimation denoted by broken lines and the green arrow in

23 Figs. 2b and 2c, respectively (approximately −0.3 m s^{-1} and 12.3 h).

1 The linear theory of inertia-gravity waves indicates that a hodograph is ellipse-shaped

2 (e.g., Shibuya et al., 2015). The lengths of major and minor axes of the hodograph ellipse

3 correspond to the amplitudes of horizontal wind components, which are parallel ($u_\parallel$) and

4 orthogonal ($u_\perp$) to the horizontal wavenumber vector ($\overrightarrow{k_h}$), respectively. The components of

5 $u_\parallel$ and $u_\perp$ are written using the zonal (u') and meridional (v') wind fluctuations:

$$u_\parallel = u' \cos \alpha + v' \sin \alpha$$
$$u_\perp = -u' \sin \alpha + v' \cos \alpha, \tag{2}$$

6 where α is the angle of $u_\parallel$ measured clockwise from the east. Based on the polarization

7 relation, the intrinsic frequency $\widehat{\omega}$ can be determined from the ratio of the lengths of the major

8 to minor axes:

$$\widehat{\omega} = \left| \frac{u_\parallel}{u_\perp} f \right|, \tag{3}$$

9 where f denotes the inertial frequency. The intrinsic frequency is taken to be positive without

10 losing generality (e.g., Sato et al., 1997).

11 The direction of the vertical energy propagation can be estimated from the rotation of the

12 hodograph in the vertical direction as follows: in the Southern Hemisphere, a counterclockwise

13 (clockwise) rotation with increasing height denotes upward (downward) energy propagation.

14 Hodographs in the vertical direction for 1200 UTC on March 22 and for 1200 UTC on March

15 23 show counterclockwise rotation (not shown), indicating upward energy propagation as also

16 shown in Fig. 4. This also means that the vertical wavenumber m is negative.

17 The horizontal wavenumber $\left| \overrightarrow{k_h} \right|$ can be indirectly estimated using the dispersion

18 relation of inertia-gravity waves, though an ambiguity for 180° remains in the direction of the

19 horizontal wavenumber vector. For hydrostatic inertia-gravity waves, the dispersion relation in

20 a uniform background is written as follows:

$$\left| \overrightarrow{k_h} \right| = \sqrt{\frac{(\widehat{\omega}^2 - f^2)m^2}{N^2}}, \tag{4}$$

1 where N is the Brunt-Väisälä frequency. Here, as a typical value, $N^2 = 3.0 \times 10^{-4}$ s^{-2} for the

2 mesosphere was used. The zonal and meridional wavenumbers (k, l) are determined as $k =$

3 $\pm|\vec{k_h}| \cos \alpha$, and $l = \pm|\vec{k_h}| \sin \alpha$, respectively. The plus-minus sign here denotes the

4 ambiguity of the wavenumber vector.

5   Figure 5 shows hodographs of the fitted sinusoidal fluctuations at heights of 70.8 km and

6 72.0 km for March 23. The intrinsic frequency and zonal and meridional wavenumbers are

7 estimated from Eqs. (3) and (4), respectively. Table 1b presents estimated wave parameters

8 resulting from the hodograph analysis. Wavenumbers are directed eastward (or westward) or

9 northeastward (or southwestward). Parameter $f/\hat{\omega}$ ranges from 0.6 to 0.85. Horizontal

10 wavelengths are longer than 1100 km, indicating that these fluctuations are due to relatively

11 large-scale inertia-gravity waves. Thus, the applied assumption on the homogeneity of

12 observed winds by dual beams (Section 2.1) is justified.

14 **4. Numerical experiment results**

15 **4.1. Simulated wave structures**

16   To examine spatial structures and generation mechanisms of the inertia-gravity waves, a

17 model simulation based on the NICAM was performed. Figure 6a shows the time-height

18 section of the simulated winds ($u \sin \theta + w \cos \theta$ (where $\theta = 10°$)) for Syowa Station from

19 00 UTC on March 17 to 00 UTC on March 24, 2015, reflecting the line-of-sight velocity of the

20 east beam of the PANSY radar system. A comparison with the observations (Fig. 2) shows that

21 the model successfully simulated synoptic-scale disturbances in the troposphere, although

22 phases of these disturbances vary slightly from observations near the end of the simulation. In

23 the lower stratosphere, a wavy structure with a small vertical wavelength of less than 1 km,

24 which was observed by the radar system from 00 UTC on March 17 to 00 UTC on March 20,

25 is hardly shown in Fig. 6a. This may be attributable to the large vertical spacing ($\Delta z = 400$ m)

26 of the model compared to such a short vertical wavelength. From the middle stratosphere to

1   the mesosphere, downward-propagating large-amplitude disturbances are dominant, which is

2   consistent with the observations. Figures 6b and 6c show the line-of-sight velocity of the east

3   beam and the zonal wind component for the same time and height sections as those reflected

4   in Figs. 2b and 2c, respectively. The amplitude of these disturbances is also comparable to that

5   of the observations; for example, the amplitude of the zonal wind component at a height of

6   about 70 km for 12 UTC on March 23 is approximately 30 m s^{-1}, which agrees with the

7   observations (see Figs. 4a and 4c).

8   Figure 7a shows the time-height section of anomalies of zonal wind components from the

9   time average at each height. As is shown in Fig. 6b, wave-like structures for the observation

10   period of about 12 h seem dominant in the mesosphere which is consistent with the radar

11   observation (Fig. 2b). Thus, we first examined diurnal and semi-diurnal migrating tidal

12   components, which are defined as components for wave period $\tau = 24$ h and zonal

13   wavenumber $s = 1$ and for $\tau = 12$ h and $s = 2$, respectively. Figure 7b shows the time-

14   height section of diurnal and semi-diurnal migrating components of zonal winds. Surprisingly,

15   these components are not dominant even in the mesosphere. Figure 7c shows the time-height

16   section of zonal wind components of planetary wave components, which are defined as

17   components with $\tau \geq 42$ h. This component does not seem to be dominant in the mesosphere.

18   Moreover, we examined the amplitude of small-scale gravity waves, which are defined as

19   components with horizontal wavelengths of less than 1000 km, as occasionally shown by

20   previous studies (e.g., Geller et al., 2013). In this study, a spatial filter is applied to the x-y

21   coordinate centered at the South Pole as projected by the Lambert azimuthal equal-area

22   projection. Figure 7d shows the time-height section of zonal wind components of the small-

23   scale gravity waves. Although these small-scale gravity waves sometimes have amplitudes that

24   exceed 20 m s^{-1} in the mesosphere, the wave structures shown in Fig. 7a are not fully explained.

25   The remaining component is shown in Fig. 7e. This component has a quite similar

1   structure and amplitude to the unfiltered anomalies shown in Fig. 7a. These results suggest that

2   dominant wave structures in the mesosphere did not form due to migrating tides, planetary

3   waves or small-scale gravity waves, but due to the remaining component. The remaining

4   component has a horizontal wavelength of greater than 1000 km and wave periods of less than

5   42 h. We further examined characteristics of the remaining component such as horizontal and

6   vertical wavenumbers and intrinsic and observed wave frequencies.

7   Figure 7e shows several large-amplitude wave packets over Syowa Station. The envelope

8   function of the wave packets is examined using an extended Hilbert transform method proposed

9   by Sato et al. (2013). An extended Hilbert transform $H[a(x,t)]$ is a fluctuation field

10   composed of a Fourier component of a particular fluctuation field $a(x,t)$ whose phase is

11   shifted by $-\pi/2$ radians. An envelope function $A_{\mathrm{env}}(x,t)$ of $a(x,t)$ is obtained using

12   $a(x,t)$ as follows:

$$A_{\mathrm{env}}(x,t) = \sqrt{a(x,t)^2 + H[a(x,t)]^2}. \qquad (5)$$

13   The extended Hilbert transform must be applied in one direction in time or space where waves

14   are fluctuating (including at least more than two wave crests). In this study, envelope functions

15   are estimated using the extended Hilbert transform of the time direction.

16   Figure 8 shows the envelope functions calculated using the extended Hilbert transform

17   applied to remaining components shown in Fig. 7e. Several large-amplitude wave packets are

18   identified and labeled as (i) to (v) for further wave parameter estimation. The observed wave

19   period and the vertical wavelength of each packet are estimated directly in Fig. 7e. The zonal

20   wavelengths and phase velocities are directly estimated using Hovmöller diagrams. Figure 9

21   shows the Hovmöller diagram at a height of 70 km at 69°S. A lot of wave packets appear not

22   only over Syowa Station throughout the simulation period, except for the initial day of the time

23   integration. It is clear that most waves propagate westward. At a longitude of roughly 40°E

24   (green dashed line) where Syowa Station is located, some dominant wave packets are found as

1   is shown in Fig. 8, corresponding to packets (i) for March 19, (ii) March 20 and (v) March 22,

2   respectively. In addition, to examine horizontal structures of the wave packets, we created

3   composite maps of zonal wind components. The grid points with local maxima of zonal wind

4   components near Syowa Station at a latitude of 69°S are chosen as a reference for the composite.

5   The composites are obtained for the time and height region denoted by the green rectangle in

6   Fig. 8, and the reference time for wave packets is determined by the center of these time periods.

7   The results of the composite analyses for packets (i) to (v) are shown in Figs. 10a to 10e,

8   respectively. It seems that wave structures are evident for all packets near Syowa Station. From

9   features observed in the time-height section, the Hovmöller diagram and the composite maps

10   of zonal wind components, we directly estimated wave parameters of horizontal wavelengths,

11   vertical wavelengths, observed frequencies, zonal phase speeds, vertical phase speeds and

12   intrinsic frequencies, which are summarized in Table 2.

13   The vertical phase speeds, observed wave periods and vertical wavelengths obtained from

14   the model simulation data agree quite well with those obtained from the PANSY radar

15   observations. Moreover, directly estimated zonal and meridional wavenumbers from the

16   simulation (Table 2) also agree quite well with those indirectly estimated from PANSY radar

17   observations using polarization and dispersion relations of inertia-gravity waves (Tables 1a and

18   1b). In addition, it is important to note that wave parameters (ω, $\vec{k}$ and m) of packets (i) to

19   (v) are consistent with the dispersion relation of the hydrostatic inertia-gravity waves:

$$\hat{\omega}^2 = (\omega - \vec{U} \cdot \vec{k})^2 = f^2 + \frac{N^2 |\vec{k}|^2}{m^2}, \tag{6}$$

20   where ω is the ground-based frequency, $\vec{k} = (k, l)$ and m are horizontal and vertical

21   components for the wavenumber vector, respectively, and $\vec{U}$ is the background horizontal

22   wind vector. Intrinsic frequencies $\hat{\omega}$ obtained from the model simulation using Eq. (6) also

23   agree with those obtained from the PANSY radar observation. From these results, we conclude

24   that dominant half-day wave period fluctuations observed in the mesosphere are likely

1   attributable to large-scale inertia-gravity waves. Hereafter, we refer to the remaining

2   component as "large-scale inertia-gravity waves."

4   **4.2. Wave propagation and generation mechanism**

5   In this section, we examine the origins of the large-scale inertia-gravity waves simulated

6   near Syowa Station. In particular, we examine disturbances occurring over wave periods of

7   close to 12 h, which were extracted by applying a bandpass filter with cutoff wave periods of

8   6 h and 24 h to large-scale inertia-gravity waves.

9   Case studies are conducted for wave packets (i) and (v), as they show clear wave structures

10   at a height of 70 km, where the PANSY radar system observed inertia-gravity waves. The

11   propagation of wave packets identified using the extended Hilbert transform method is

12   manually traced. Three dimensional spatial locations of the wave packets are determined by

13   the maxima of the envelope function for each time. Hereafter, we refer to this method as

14   "manual wave packet tracing."

15   Our approach to manual wave packet tracing for packet (v) is shown in Figure 11a, which

16   depicts a horizontal map of zonal wind components of the large-scale inertia-gravity waves and

17   their envelope functions for 03 UTC on March 23. Significant disturbances of high amplitude

18   are found near Syowa Station corresponding to packet (v). The location of a local maximum of

19   the envelope function (the green circle in Fig. 11a) is defined as the center of packet (v) when

20   the envelope function of packet (v) has its local maximum in the Hovmöller diagram at 69°S

21   (Fig. 11b). Figures 11c and 11d show the results for packet (i).

22   Figures 12a-d show the times and spatial locations of packet (v) at heights of 60 km, 40

23   km, 25 km and 23 km, respectively. It appears that the location of packet (v) is successfully

24   traced backward from a height of 70 km to 23 km, suggesting that packet (v) observed over

25   Syowa Station in the mesosphere propagated from the lower stratosphere at roughly (100°E,

26   40°S). At heights of 25 km to 23 km, the vertical propagation of packet (v) is quite slow

1   compared to that in the upper stratosphere and mesosphere.

2   Figures 12e to 12 g show the times and spatial locations of packet (i) at heights of 63 km,

3   58 km, 53 km and 48 km, respectively. At heights of 70 km, 63 km and 58 km, the green circles

4   seem to trace the same wave structures. However, as we cannot trace packet (i) below a height

5   of 53 km, the wave structure becomes obscured at heights of 53 km and 48 km.

6   To confirm the validity of the manual wave packet tracing results, we conducted a

7   backward ray tracing analysis of the large-scale inertia-gravity wave (e.g., Marks and

8   Eckermann 1995). We used the wave parameters of packets (i) and (v) shown in Table 2 as

9   initial parameters for the ray tracing analysis. The average of the model output for March 17 to

10 March 23 is used as the background wind for the ray tracing analysis. Figure 13 and Table 3

11 summarize the manual packet and ray tracing results. The times and spatial locations of packet

12 (v) detected by the manual packet tracing agree with those obtained by idealized ray tracing,

13 although not for the lower stratosphere. However, the tracing of packet (i) agrees well with

14 those by idealized ray tracing results at above 58 km, where clear wave structures are shown

15 in the horizontal map. These findings support the validity of manual wave packet tracing based

16 on the extended Hilbert transform and ray tracing based on inertia-gravity wave theory.

17   The source of the inertia-gravity waves can be located at any altitude along the ray above

18 the lowest traceable altitude. Thus, we further examine possible sources of packets (i) and (v)

19 along the ray shown in Fig. 13. First, we focus on the ray of packet (v) in the lower stratosphere.

20 Figure 14 shows the longitude-height section of background winds below z = 18 km and of

21 disturbances above z = 19 km at 40°S for 03 UTC on March 21. At roughly 100°E longitude,

22 wave disturbances appear to be captured over the core of the tropospheric jet stream. This

23 feature is quite similar to the gravity waves generated by the spontaneous radiation from the

24 large-scale jet in the tropopause (e.g., O'Sullivan and Dunkerton, 1995; Plougonven and

25 Synder 2007; Yasuda et al., 2015a, b). The long propagation time in the lower stratosphere may

1   be related to the wave capture mechanism (Bühler and McIntyre, 2005; Shibuya et al., 2015).

2   To explore such a possibility, a horizontal map of the residual of the nonlinear balance

3   equation (ΔNBE; Zhang et al., 2001), which is an index showing the degree of flow imbalance,

4   is examined. Here, ΔNBE is defined as follows:

$$\Delta NBE = 2J(u,v) + f\varsigma - \alpha\nabla^2 P \qquad (7)$$

5   where ς, α, and P denote the relative vorticity, specific volume and pressure level,

6   respectively. The Jacobian term is $J(u,v) = \partial u/\partial x \times \partial v/\partial y - \partial v/\partial x \times \partial u/\partial y$. To exclude

7   possible contaminations of ΔNBE by small-scale gravity waves, we apply a low-pass filter in

8   the zonal and meridional directions with a cutoff length of 1000 km in advance. Figure 15

9   shows horizontal maps of the absolute value of the horizontal wind and ΔNBE at a height of

10   10 km for 03 UTC on March 21. The absolute value of the horizontal wind is also denoted by

11   thick contours. It is clear that large values are observed in ΔNBE around the tropospheric jet

12   meandering around (110°E, 40°S), where packet (v) was located. This feature not only suggests

13   that the imbalance in the tropospheric jet was significant but also that packet (v) may have been

14   generated by the spontaneous radiation mechanism.

15   Next, we examined a possible generation mechanism for packet (i). The disappearance of

16   the clear wave structure at a height of 53 km (Figs. 12f and 12g) may indicate that the source

17   of packet (i) is found at this height. To confirm this possibility, we examined fluctuation

18   characteristics and background zonal winds of the upper stratosphere. Figure 16 shows a

19   longitude-height cross-section of fluctuation components ($\sqrt{\rho_0}u'$) and the background zonal

20   wind at 15 UTC on March 18 at 69°S. The background zonal wind is obtained using a low-

21   pass filter with a cutoff zonal wavelength of approximately 5,000 km.

22   Interestingly, it seems that fluctuations show symmetric features above and below the core

23   of the polar night jet at a height of 50 km. The height at which packet (i) becomes obscured

24   roughly corresponds to the core of the polar night jet (Figs. 12f and 12g). These results imply

1   that fluctuations are generated at a height close to the core of the polar night jet. To confirm

2   this, we examined the vertical profile of the energy flux $\overline{p'w'}$ (Fig. 16b). The average was

3   calculated for the longitudinal region spanning from -90°E to 60°E. The energy flux is upward

4   above and downward below the core of the polar night jet. This result supports the hypothesis

5   that packet (i) was generated at a height close to the core of the polar night jet.

6   A plausible generation mechanism of inertia-gravity waves in the upper stratosphere is

7   spontaneous radiation from the polar night jet (e.g., Sato and Yoshiki, 2008). It is also worth

8   noting that observational studies show high percentages of downward gravity wave

9   propagation in the polar stratosphere compared to those found at low and middle latitudes (e.g.,

10 Yoshiki and Sato, 2000; Guest et al., 2000; Moffat-Griffin et al., 2013; Murphy et al., 2014;

11 Mihalikova et al., 2016). Thus, a horizontal map of the absolute value of horizontal winds and

12 ΔNBE is examined at a height of 55 km for 15 UTC on March 18 for the present case. However,

13 the polar night jet did not meander considerably, and ΔNBE was not large (not shown).

14   The symmetric structure of inertia-gravity waves shown in Fig. 16a is quite similar to that

15 described in theoretical studies of inertia-gravity waves radiated by spontaneous radiation from

16 a balanced flow (Yasuda et al., 2015b: their Figure 6). Yasuda et al. (2015a, b) theoretically

17 discussed the spontaneous radiation mechanism of gravity waves in terms of the quasi-

18 resonance of gravity waves with a secondary circulation component slaved to a balanced flow.

19 Quasi resonance occurs when time and spatial scales of gravity waves are partially comparable

20 to those of the slaved component. This indicates that the spontaneous radiation of gravity waves

21 can occur even when the absolute value of ΔNBE is not large. Thus, packet (i) may be radiated

22 by such a quasi-resonance mechanism in the polar night jet.

23   We examined sources of wave packets (ii), (iii) and (iv) and of other wave packets that

24 are dominant at different longitudes (Fig. 9). Our results suggest that other wave packets were

25 also generated by spontaneous radiation from the upper tropospheric jet stream or from the

1   polar night jet stream.

3   **5. Discussion**

4   As is shown in Section 4, wave structures with large amplitudes in the lower mesosphere

5   (below 80 km) with the ground-based period of quasi 12 h are likely attributable to large-scale

6   inertia-gravity waves. The horizontal wavelengths of quasi 12 h inertia-gravity waves range

7   from 1500 km to 2500 km as shown in Table 2. This conclusion diverges from suggestions

8   made in previous studies, which posit that 12 h disturbances can be either migrating semi-

9   diurnal tides of zonal wavenumber two or non-migrating semi-diurnal tides of zonal

10   wavenumber one. This difference can be attributed to the difference in observed height regions

11   as follows: height regions examined in this study include the upper stratosphere and lower

12   mesosphere below 80 km while those examined in previous studies include the mesosphere

13   located above 85 km. The behaviors of quasi 12 h inertia-gravity waves above 80 km should

14   be examined further in future studies.

15   Large-scale inertia-gravity waves with horizontal wavelengths of longer than 1000 km in

16   the mesosphere have already been reported in several studies (Li et al., 2007; Lu et al., 2009,

17   Nicolls et al., 2010; Chen et al., 2013). For example, Nicolls et al. (2010), using the Poker Flat

18   Incoherent Scatter Radar system, found large-amplitude coherent wave packets with wave

19   periods of roughly 10.5 h and horizontal wavelengths of 700 km to 1600 km in the mesosphere.

20   Nicolls et al. (2010) cited jet stream adjustment in the tropopause as a potential source. Chen

21   et al. (2013) also estimated a source for one inertia-gravity wave with a horizontal wavelength

22   of 2200 km, a period of 7.7 hour and a vertical wavelength of 22 km, which was observed in

23   the Antarctic mesopause region by combined Fe lidar/MF radar measurements. They

24   heuristically traced the inertia-gravity wave back to a region of unbalanced flow in the

25   stratosphere (z ~ 43 - 46 km). However, no previous studies have directly examined sources of

26   these large-scale inertia-gravity waves in the mesosphere using a numerical model. This study

1   examines the propagation of such large-scale inertia-gravity waves and generation by

2   spontaneous radiation from the polar night jet and tropospheric jet, combining the observational

3   data and numerical simulation outputs.

4   We have further examined vertical fluxes of zonal and meridional momentum associated

5   with large-scale inertia-gravity waves $\rho_0 \overline{u'w'}$ and $\rho_0 \overline{v'w'}$. The overbar denotes a zonal

6   averaging operation. Figures 17a and 17b show latitude-height sections of $\rho_0 \overline{u'w'}$ and $\rho_0 \overline{v'w'}$,

7   respectively, which are averaged for March 19 to March 23 2015. Large negative $\rho_0 \overline{u'w'}$ and

8    $\rho_0 \overline{v'w'}$ values are distributed approximately 40°S in the lower stratosphere and approximately

9   75°S in the mesosphere. The signs of $\rho_0 \overline{u'w'}$ and $\rho_0 \overline{v'w'}$ are consistent with parameter

10   estimations from PANSY radar observations and from the numerical simulation. The slanted

11   structures seem quite similar to the propagation path of packet (v) discussed in Section 4.2.

12   Such a slanted structure is likely formed from the meridional propagation of inertia-gravity

13   waves, which is numerically shown and theoretically discussed by Sato et al. (2009) and Sato

14   et al. (2012) in terms of refraction and advection by background wind.

15   Interestingly, Fig. 17a shows that the value of $\rho_0 \overline{u'w'}$ is lower in the middle stratosphere,

16   thus showing a peak of negative $\rho_0 \overline{u'w'}$ in the mesosphere. Small-scale gravity waves do not

17   follow such a pattern (not shown). This result suggests that parts of large-scale inertia-gravity

18   waves are generated in the upper stratosphere as discussed in Section 4.2. In contrast, such a

19   feature is not observed in $\rho_0 \overline{v'w'}$, although a small negative local maximum is present at

20   heights of 50 km to 55 km at approximately 60°S. This result implies that wavenumber vectors

21   of inertia-gravity waves in the mesosphere tend to move eastward, consistent with the

22   parameter estimation shown in Section 4.1.

23   Next, we examined the energy of the large-scale inertia-gravity waves by dividing into the

24   following three components: horizontal wind kinetic energy ($\overline{KE}$), vertical wind kinetic energy

25   ($\overline{VE}$) and potential energy ($\overline{PE}$):

$$\overline{KE} = \frac{1}{2}\rho_0\left(\overline{u'^2} + \overline{v'^2}\right), \tag{8}$$

$$\overline{VE} = \frac{1}{2}\rho_0\overline{w'^2}, \tag{9}$$

and $$\overline{PE} = \frac{1}{2}\rho_0\frac{g^2}{N^2}\overline{\left(\frac{T'}{T}\right)^2}. \tag{10}$$

1 According to the linear theory of hydrostatic inertia-gravity waves, the ratio of $\overline{VE}$ to $\overline{PE}$ has

2 the following relation (from the thermodynamic equation) (e.g., Wang et al., 2005; Geller and

3 Gong 2010, Geller et al., 2013);

$$\frac{\overline{VE}}{\overline{PE}} = \frac{\widehat{\omega}^2}{N^2}. \tag{11}$$

4 Thus, $|f/\widehat{\omega}|$ can be derived as follows:

$$\left|\frac{f}{\widehat{\omega}}\right| = \left|\frac{f}{N}\right|\sqrt{\frac{\overline{PE}}{\overline{VE}}}. \tag{12}$$

5 Figure 17c shows the latitude-height section of $|f/\widehat{\omega}|$. In the mesosphere, $|f/\widehat{\omega}|$ ranges

6 from 0.6 to 0.8 at approximately 70°S, which agrees quite well with estimates from the

7 hodograph analysis (Tables 1 and 2). The fact that $|f/\widehat{\omega}|$ has higher values than 0.6 indicates

8 that the large-scale inertia-gravity waves are almost hydrostatic. Note that the value of $|f/\widehat{\omega}|$

9 is larger than 1.0 in the lower stratosphere, which is inconsistent with the linear theory of

10 inertia-gravity waves. This implies that the large-scale inertia-gravity waves defined in Section

11 4.1 include balanced components in the lower stratosphere (e.g., baroclinic wave components)

12 as well as large-scale inertia-gravity waves.

13 Figures 17d and 17e show latitude-height sections of $\overline{KE}$ and $\overline{PE}$ for the large-scale

14 inertia-gravity waves. The slanted structures in Figs. 17a and 17b are also shown in Figs. 17d

15 and 17e. It should be noted that the ratio of the Coriolis parameter to the intrinsic frequency

16 $(f/\widehat{\omega})$ can also be obtained from $\overline{KE}$ and $\overline{PE}$ as follows:

$$\left|\frac{f}{\hat{\omega}}\right| = \sqrt{\frac{\frac{KE}{PE} - 1.}{\frac{KE}{PE} + 1}}. \tag{13}$$

1 We confirmed that $(f/\hat{\omega})$ values obtained by Eq. (13) are consistent with the result obtained

2 from Eq. (12) (not shown).

4 **6. Summary**

5   The first observation with a complete system of the PANSY radar were successfully

6 performed for March 16 – 24, 2015. During this period, quasi 12 h disturbances in the

7 mesosphere at heights of 70 km to 80 km were detected by the PANSY radar system. Our main

8 results are summarized as follows:

9   1)   The observed wave period and vertical wavelength are about 12.3 h and 13.8

10   km, respectively. The estimated horizontal wavelength is longer than 1100 km. The

11   wavenumber vectors tend to be directed northeastward or southwestward. Ratios of the

12   Coriolis parameter to the intrinsic frequency range from 0.6 to 0.85.

13   2)   Moreover, using the non-hydrostatic numerical model with a model top of 87

14   km, we succeeded in simulating quasi 12 h disturbances in the mesosphere. Using time

15   and spatial filters, we found that quasi 12 h disturbances are not attributable to semi-

16   diurnal migrating tides, but to large-scale inertia-gravity waves with horizontal

17   wavelengths of longer than 1400 km. Wavenumber vectors simulated in the NICAM are

18   directed northeastward. Wave parameters directly estimated using the NICAM agree

19   quite well with those estimated by the PANSY radar observation system.

20   3)   The detected inertia-gravity waves were likely generated by the spontaneous

21   radiation mechanism of the mid-latitude upper tropospheric jet at the tropopause or the

22   polar night jet. Inertia-gravity waves generated near the mid-latitude tropopause

23   propagate laterally and vertically to the polar mesosphere. Refraction and/or advection

1   by background winds are essential for lateral propagation.

2   4)   Vertical fluxes of the zonal and meridional momentum of large-scale inertia-

3   gravity waves show a slanted structure from the mid-latitude lower stratosphere to the

4   polar mesosphere. Moreover, the vertical flux of the zonal momentum shows a strong

5   negative peak in the mesosphere, suggesting the generation of large-scale inertia-gravity

6   waves in the upper stratosphere.

7   The present study offers a quantitative discussion based on high-resolution observations

8 and numerical models. Statistical analyses of large-scale inertia-gravity waves in the real

9 atmosphere will be of interest as future studies using observations and numerical simulations

10 in the different seasons.

7. Data availability

13 The PANSY radar observation data is available at the project website, http://pansy.eps.s.u-

14 tokyo.ac.jp. Model outputs are available on request from the corresponding author.

8. Competing interest

17 The authors declare that they have no conflict of interest.

Acknowledgements

20 The PANSY multi-institutional project operated by the University of Tokyo and the National

21 Institute of Polar Research (NIPR), and the PANSY radar system was operated by the

22 Japanese Antarctic Research Expedition. We thank Takuji Nakamura for his many useful

23 comments and discussions. We also thank Arata Amemiya for describing the idealized ray

24 tracing model. Numerical simulations were run on the NIPR supercomputer. All figures

25 shown in this paper were created using the Dennou Club Library (DCL). This study was

26 supported by the Program for Leading Graduate Schools, MEXT, Japan. The study was also

1   supported through the Japan Society for the Promotion of Science (JSPS) Grant-in-Aid

2   Scientific Research (A) 25247075 (Kaoru Sato) and Grant-in-Aid for Research Fellow (26-

3   9257) (Ryosuke Shibuya) programs.

5   **References**

6   Akmaev, R. A., J. M. Forbes, F.-J. Lübken, D. J. Murphy, and J. Höffner, 2016: Tides in the

7   mesopause region over Antarctica: Comparison of whole atmosphere model simulations

8   with ground-based observations, *J. Geophys. Res. Atmos.*, **121**, 1156–1169, doi:10.1002/

9   2015JD023673.

10   Alexander, M. J., M. Geller, C. McLandress, S. Polavarapu, P. Preusse, F. Sassi, K. Sato, S.

11   Eckermann, M. Ern, A. Hertzog, Y. Kawatani, M. Pulido, T. Shaw, M. Sigmond, R.

12   Vincent, S. Watanabe, 2010: Recent developments in gravity wave effects in climate

13   models, and the global distribution of gravity wave momentum flux from observations

14   and models, *Q. J. Roy. Meteorol. Soc.*, **136**, 1103-1124.

15   Aso, T., 2007: A note on the semidiurnal non-migrating tide at polar latitudes, *Earth Planets

16   Space*, **59**, e21–e24.

17   Baldwin, M. P., and Coauthors, 2003: The Quasi-Biennial Oscillation, *Rev. Geophys.*, **39**,

18   179-229.

19   Becker, E., 2009: Sensitivity of the upper mesosphere to the Lorenz energy cycle of the

20   troposphere, *J. Atmos. Sci.*, **66**, 647–666, doi: 10.1175/2008JAS2735.1.

21   Bloom, S., L. Takacs, A. DaSilva, and D. Ledvina, 1996: Data assimilation using incremental

22   analysis updates. *Mon. Wea. Rev.*, **124**, 1256–1271.

23   Bühler, O., and M. E. McIntyre, 2005: Wave capture and wave-vortex duality. *J. Fluid.

24   Mech.,* **534,** 67-95.

25   Chen, C., X. Chu, A. J. McDonald, S. L. Vadas, Z. Yu, W. Fong, and X. Lu, 2013: Inertia‐

26   gravity waves in Antarctica: A case study using simultaneous lidar and radar

1 measurements at McMurdo/Scott Base (77.8° S, 166.7° E). *Journal of Geophysical*

2 *Research: Atmospheres*, **118**(7), 2794-2808.

3 Chu, X., W. Huang, F. Fong, Z. Yu, Z. Wang, J. A. Smith, and C. S. Gardner 2011: First lidar

4 observations of polar mesospheric clouds and Fe temperatures at McMurdo (77.8°S,

5 166.7°E), Antarctica, *Geophys. Res. Lett.*, **38**, L16810, doi:10.1029/2011GL048373.

6 Collins, R. L., D. C. Senft, and C. S. Gardner 1992: Observations of a 12 H wave in the

7 mesopause region at the South Pole, *Geophys. Res. Lett.*, **19**(1), 57–60,

8 doi:10.1029/91GL02780.

9 Eyring, V., T. G. Shepherd, and D. W. Waugh, Eds., 2010: SPARC CCMVal report on the

10 evaluation of chemistry-climate models. SPARC Rep. 5, WCRP-132, WMO/TD-No.

11 1526, 434 pp.

12 Fisher, G. M., R. J, Niciejewski, T. L. Killeen, W. A. Gault, G. G. Shepherd, S. Brown, and

13 Q. Wu, 2002: Twelve‐hour tides in the winter northern polar mesosphere and lower

14 thermosphere. *Journal of Geophysical Research: Space Physics*, **107**(A8).

15 Fraser, G. J. and U. Khan, 1990: Semidiurnal variations in the time scale of irregularities near

16 the Antarctic summer mesopause. *Radio science*, **25**(5), 997-1003.

17 Forbes, J. M., N. A. Makarov, and Y. I. Portnyagin, First results from the meteor radar at

18 south pole: A large 12-hour oscillation with zonal wavenumber one, *Geophys. Res. Lett.,*

19 **22,** 3247– 3250, 1995.Forbes, J.M.,

20 Forbes, J. M., Y. I. Portnyagin, N. A. Markov, S. E. Palo, E. G. Merzlyakov and X. Zhang,

21 1999: Dynamics of the lower thermosphere over South Pole from meteor radar

22 windmeasurements. *Earth Planets Space,* **51**, 611–620.

23 Fritts, D. C., D. M. Riggin, B. B. Balsley, and R. G. Stockwell 1998: Recent results with an

24 MF radar at McMurdo, Antarctica: Characteristics and variability of motions near 12-

25 hour period in the mesosphere, *Geophys. Res. Lett.*, **25**(3), 297–300,

1 doi:10.1029/97GL03702.

2 Fritts , D. C. and M. J. Alexander, 2003: Gravity wave dynamics and effects in the middle

3 atmosphere. *Rev. Geophys.*, **41**, 1003, doi:10.1029/2001RG000106.

4 Geller, M. A. and J. Gong, 2010: Gravity wave kinetic, potential, and vertical fluctuation

5 energies as indicators of different frequency gravity waves. *Journal of Geophysical*

6 *Research: Atmospheres*, **115**(D11).

7 Geller, M. A., M. Alexander, P. T. Love, J. Bacmeister, M. Ern, A. Hertzog, T. Zhou, 2013: A

8 Comparison between Gravity Wave Momentum Fluxes in Observations and Climate

9 Models. *Journal of Climate*, **26**(17).

10 Guest, F. M., M. J. Reeder, C. J. Marks, and D. J. Karoly (2000), Inertia-gravity waves

11 observed in the lower stratosphere over Macquarie Island, *J. Atmos. Sci.*, **57**, 737–752.

12 Hagan, M. E., and J. M. Forbes, 2003: Migrating and nonmigrating semidiurnal tides in the

13 upper atmosphere excited by tropospheric latent heat release, *J. Geophys. Res.,* **108(A2)**,

14 1062, doi:10.1029/2002JA009466.

15 Haynes, P. H., 1998: The latitudinal structure of the quasi-biennial oscillation. *Quart. J. Roy.*

16 *Meteor. Soc.,* **124,** 2645-2670.

17 Hernandez, G., G. J. Fraser, and R. W. Smith 1993: Mesospheric 12-hour oscillation near

18 South Pole, Antarctica, *Geophys. Res. Lett.*, **20**(17), 1787–1790,

19 doi:10.1029/93GL01983.

20 Hertzog, A., G. Boccara, R. A. Vincent, F. Vial, and P. Cocquerez, 2008: Estimation of

21 gravity wave momentum flux and phase speeds from quasi-Lagrangian stratospheric

22 balloon flights. Part II: Results from the Vorcore campaign in Antarctica. *Journal of the*

23 *Atmospheric Sciences*, **65**(10), 3056-3070.

24 Hirota, I. and T. Niki, 1986: Inertia-gravity waves in the troposphere and stratosphere

25 observed by the MU radar. *J. Meteor. Soc. Japan,* **64**, 995−999.

1   Kataoka, R., D. Shiota, E. Kilpua, and K. Keika 2015: Pileup accident hypothesis of magnetic

2   storm on 17 March 2015, *Geophys. Res. Lett.*, **42**, 5155–5161,

3   doi:10.1002/2015GL064816.

4   Kohma, M. and K. Sato, 2011: The effects of atmospheric waves on the amounts of polar

5   stratospheric clouds. *Atmos. Chem. Phys.,* **11**, 11535-11552, doi:10.5194/acp-11-11535-

6   2011.

7   Lane, T. P., J. D. Doyle, R. Plougonven, M. A. Shapiro, and R. D. Sharman, 2004:

8   Observations and numerical simulations of inertia-gravity waves and shearing

9   instabilities in the vicinity of a jet stream. *J. Atmos. Sci.,* **61**, 2792-2706.

10   Li, T., C.-Y. She, H.-L. Liu, T. Leblanc, and I. S. McDermid, 2007: Sodium lidar–observed

11   strong inertia-gravity wave activities in the mesopause region over Fort Collins,

12   Colorado (41°N, 105°W), *J. Geophys. Res.*, **112**, D22104, doi:10.1029/2007JD008681.

13   Liu, H. L., J. M. McInerney, S. Santos, P. H. Lauritzen, M. A. Taylor, and N. M. Pedatella,

14   2014: Gravity waves simulated by high‐resolution Whole Atmosphere Community

15   Climate Model. *Geophysical Research Letters*, **41(24)**, 9106-9112.

16   Lu, X., A. Z. Liu, G. R. Swenson, T. Li, T. Leblanc, and I. S. McDermid, 2009: Gravity wave

17   propagation and dissipation from the stratosphere to the lower thermosphere, *J.*

18   *Geophys. Res.*, **114**, D11101, doi:10.1029/2008JD010112.

19   Marks, C. J., and S. D. Eckermann, 1995: A three-dimensional nonhydrostatic ray tracing

20   model for gravity waves: Formulation and preliminary results for the middle

21   atmosphere. *J. Atmos. Sci*., **52**(11), 1959-1984.

22   Mayr, H. G., J. G. Mengel, E. R. Talaat, H. S. Porter, and K. L. Chan, 2005a: Mesospheric

23   non-migrating tides generated with planetary waves: I. Characteristics, *J. Atmos. Sol.*

24   *Terr. Phys.,* **67**, 959– 980.

25   Mayr, H. G., J. G. Mengel, E. R. Talaat, H. S. Porter, and K. L. Chan, 2005b: Mesospheric

non-migrating tides generated with planetary waves: II. Influence of gravity waves, *J. Atmos. Sol. Terr. Phys.,* **67**, 981–991.

McDonald, A. J., S. E. George, and R. M. Woollands, 2009: Can gravity waves significantly impact PSC occurrence in the Antarctic?, *Atmos. Chem. Phys.*, **9**, 8825–8840, doi:10.5194/acp-9-8825-2009.

McLandress, C., T. G. Shepherd, S. Polavarau, S. R. Beagley, 2012: Is Missing Orographic Gravity Wave Drag near 60°S the Cause of the Stratospheric Zonal Wind Biases in Chemistry–Climate Models?. *J. Atmos. Sci.,* **69**, 802–818, 2012.

McFarlane, N. A., 1987: The effect of orographically excited wave drag on the general circulation of the lower stratosphere and troposphere. *J. Atmos. Sci.*, **44**, 1775–1800.

Mihalikova, M., Sato, K., Tsutsumi, M., and Sato, T, 2016.: Properties of inertia-gravity waves in the lowermost stratosphere as observed by the PANSY radar over Syowa Station in the Antarctic, Ann. Geophys., 34, 543-555, doi:10.5194/angeo-34-543-2016.

Moffat-Griffin, T., M. J. Jarvis, S. R. Colwell, A. J. Kavanagh, G. L. Manney, and W. H. Daffer (2013), Seasonal variations in the lower stratospheric gravity wave energy above the Falkland Islands, *J. Geophys. Res. Atmos.*, **118**, 10,861–10,869, doi:10.1002/jgrd.50859.

Murphy, D. J., et al., 2006: A climatology of tides in the Antarctic mesosphere and lower thermosphere, *J. Geophys. Res.*, **111**, doi:10.1029/2005JD006803.

Murphy, D. J., T. Aso, D. C. Fritts, R. E. Hibbins, A. J. McDonald, D. M. Riggin, M. Tsutsumi, and R. A. Vincent, 2009: Source regions for Antarctic MLT non-migrating semidiurnal tides, *Geophys. Res. Lett.*, **36**, L09805, doi:10.1029/2008GL037064.

Murphy, D. J., S. P. Alexander, A. R. Klekociuk, P. T. Love, and R. A. Vincent, 2014: Radiosonde observations of gravity waves in the lower stratosphere over Davis, Antarctica. J. Geophys. Res. Atmos., 119, 11 973–11 996, doi:10.1002/ 2014JD022448.

1   Nakamura, T., T. Tsuda, M. Yamamoto, S. Fukao, and S. Kato 1993: Characteristics of

2   gravity waves in the mesosphere observed with the middle and upper atmosphere radar

3   2. Propagation direction, *J. Geophys. Res.*, **98**(D5), 8911–8923, doi:10.1029/92JD03030.

4   Nakanishi M. and H. Niino, 2004: An Improved Mellor–Yamada Level-3 Model with

5   Condensation Physics: Its Design and Verification. *Boundary-Layer Meteorol.* **112**,1–31

6   Nastrom, G. D., and F. D. Eaton 2006: Quasi-monochromatic inertiagravity waves in the

7   lower stratosphere from MST radar observations, *J. Geophys. Res.*, **111**, D19103,

8   doi:10.1029/2006JD007335.

9   Nicolls, M. J., R. H. Varney, S. L. Vadas, P. A. Stamus, C. J. Heinselman, R. B. Cosgrove,

10   and M. C. Kelley 201:, Influence of an inertia-gravity wave on mesospheric dynamics: A

11   case study with the Poker Flat Incoherent Scatter Radar, *J. Geophys. Res.*, **115**, D00N02,

12   doi:10.1029/2010JD014042.

13 Okamoto, K., K. Sato, and H. Akiyoshi, 2011: A study on the formation and trend of the

14   Brewer-Dobson circulation. *J. Geophys. Res.*, **116,** D10117, doi:10.1029/2010JD014953.

15 O'Sullivan, D. J., and T. J. Dunkerton, 1995: Generation of inertia-gravity waves in a

16   simulated life cycle of baroclinic instability. *J. Atmos. Sci.,* **52,** 3695-3716.

17 Pavelin, E. G., J. A. Whiteway, and G. Vaughan, Observation of gravity wave generation and

18   breaking in the lowermost stratosphere, 2001: *J. Geophys. Re*s., **106**, 5173 – 5179.

19 R. Plougonven and C. Snyder, 2007: Inertia-gravity waves spontaneously generated by jets

20   and fronts. Part I: Different baroclinic life cycles. *J. Atmos. Sci.,* **64**, p2502-2520.

21 Plumb, R. A., 2002: Stratospheric transport. *J. Meteor. Soc. Japan,* **80,** 793-809.

22 Portnyagin, Y. I., J. M. Forbes, N. A. Makarov, E. G. Merzlyakov, and S.Palo, The

23   summertime 12-h wind oscillation with zonal wavenumber s =1 in the lower

24   thermosphere over the South Pole, *Ann. Geophys.*, **16**,828– 837, 1998.

25 Richter, J. H., F. Sassi, and R. R. Garcia, 2009: Toward a physically based gravity wave

1 source parameterization in a general circulation model, *J. Atmos. Sci.,* **67**, 136–156.

2 Rienecker, M., and Coauthors, 2011: MERRA: NASA's ModernEra Retrospective Analysis

3 for Research and Applications. *J. Climate*, **24**, 3648–3624.

4 Riggin, D. M., D. C. Fritts, M. J. Jarvis, G. O. L. Jones, 1999: Spatial structure of the 12-hour

5 wave in the Antarctic as observed by radar. *Earth Planets and Space*, **51**, 621–628.

6 Sato, K., 1994: A statistical study of the structure, saturation and sources of inertio-gravity

7 waves in the lower stratosphere observed with the MU radar.

8 *J. Atmos. Terr. Phys.,* **56,** 755-774.

9 Sato, K., T. Kinoshita, and K. Okamoto, 2013: A new method to estimate three-dimensional

10 residual mean circulation in the middle atmosphere and its application to gravity-wave

11 resolving general circulation model data, *J. Atmos. Sci.,* **70**, 3756–3779.

12 doi: http://dx.doi.org/10.1175/JAS-D-12-0352.1.

13 Sato, K., D. J. O'Sullivan, and T. J. Dunkerton, 1997: Low-frequency inertia-gravity waves in

14 the stratosphere revealed by three-weak continuous observation with the MU radar.

15 *Geophys. Res. Lett.*, **24,** 1739-1742.

16 Sato, K., and T. J. Dunkerton, 1997: Estimates of momentum flux associated with equatorial

17 Kelvin and gravity waves. *J. Geophys. Res.,* **102**, 26,247-26,261.

18 Sato, K., M. Tsutsumi, T. Sato, T. Nakamura, A. Saito, Y. Tomikawa, K. Nishimura, M.

19 Kohma, H. Yamagishi, and T. Yamanouchi, 2014: Program of the Antarctic Syowa

20 MST/IS Radar (PANSY), *J. Atmos. Solar-Terr. Phys.*, **118A**, 2-15, 2014.

21 Sato, K., S. Watanabe, Y. Kawatani, Y. Tomikawa, K. Miyazaki, and M. Takahashi, 2009:

22 On the origins of mesospheric gravity waves, *Geophys. Res. Lett.,* **36,** L19801,

23 doi:10.1029/2009GL039908.

24 Sato, K., S. Tateno S. Watanabe, and Y. Kawatani (2012), Gravity wave characteristics in the

25 Southern Hemisphere revealed by a high-resolution middle-atmosphere general

1   circulation model. *J. Atmos. Sci.*, **69**, 1378–1396, doi:10.1175/JAS-D-11-0101.1.

2   Sato, K., and M. Yoshiki, 2008: Gravity wave generation around the polar vortex in the

3   stratosphere revealed y 3-houly radiosonde observations at Syowa Station. *J. Atmos.*

4   *Sci.,* **65,** 3719-3735.

5   Sato, K., and M. Yamada, 1994: Vertical structure of atmospheric gravity waves revealed by

6   the wavelet analysis. *Journal of Geophysical Research: Atmospheres (1984–*

7   *2012)*, **99**(D10), 20623-20631.

8   Satoh, M., T. Matsuno, H. Tomita, H. Miura, T. Nasuno, and S. Iga, 2008: Nonhydrostatic

9   icosahedral atmospheric model (NICAM) for global cloud resolving simulations. *J.*

10   *Comput. Phys.*, the special issue of Predicting Weather, Climate and Extreme Events,

11   **227**, 3486−3514, doi: 10.1016/j.jcp.2007.02.006.

12   Satoh, M., Tomita, H., Yashiro, H., Miura, H., Kodama, C., Seiki, T., Noda, A. T., Yamada, Y.,

13   Goto, D., Sawada, M., Miyoshi, T., Niwa, Y., Hara, M., Ohno, T., Iga, S., Arakawa, T.,

14   Inoue, T., Kubokawa, H., 2014: The Non-hydrostatic Icosahedral Atmospheric Model:

15   Description and Development. *Progress in Earth and Planetary Science,* 1, **18**.

16   doi:10.1186/s40645-014-0018-1

17   Scinocca, J. F., 2003: An accurate spectral nonorographic gravity wave drag parameterization

18   for general circulation models. *J. Atmos. Sci.,* **60,** 667-682.

19   Shibata, T., K. Sato, H. Kobayashi, M. Yabuki, and M. Shiobara, 2003: The Antarctic polar

20   stratospheric clouds under the temperature perturbation by nonorogaphic inertia-gravity

21   waves observed by micropulse lidar. *J. Geophys. Res.,* **108,** 4105,

22   doi:10.1029/2002JD002713.

23   Shibuya R., H. Miura and K. Sato, 2016: A grid transformation method for a quasi-uniform,

24   circular fine region using the spring dynamic, *Journal of the Meteorological Society of*

25   *Japan*, 94, doi:10.2151/jmsj.2016-022.

1   Shibuya, R., K. Sato, Y. Tomikawa, M. Tsutsumi and T. Sato, 2015: A study of multiple

2   tropopause structures caused by inertia-gravity waves in the Antarctica, *J. Atmos. Sci.*,

3   **72**, 2109–2130.

4   Stolarski, R. S., A. R. Douglass, M. Gupta, P. A. Newman, S. Pawson, M. R. Schoeberl, and

5   J. E. Nielsen, 2006: An ozone increase in the Antarctic summer stratosphere: A

6   dynamical response to the ozone hole. *Geophys. Res. Lett.,* **33,** L21805,

7   doi:10.1029/2006GL026820.

8   Talaat, E. R., and H.G. Mayr, 2011: Model of semidiurnal pseudo tide in the high-latitude

9   upper mesosphere, *Journal of Atmospheric and Solar-Terrestrial Physics,* **73**, 2386–

10   2391

11 Tomita, H., M. Satoh, K. Goto, 2002: An optimization of icosahedral grid by using spring

12   dynamics. *J. Comp. Phys.*, **183**, 307-331.

13 Vaughan, G., and R. M. Worthington 2007: Inertia-gravity waves observed by the UK MST

14   radar, *Q. J. R. Meteorol. Soc.*, **133**: (S2) 179–188.

15 Vincent, R. A., I. M. Reid, 1983: HF Doppler Measurements of Mesospheric Gravity Wave

16   Momentum Fluxes. *J. Atmos. Sci.*, **40**, 1321–1333. doi: 10.1175/1520-

17   0469(1983)040<1321:HDMOMG>2.0.CO;2

18 Walterscheid, R. L., G. G. Sivjee, G. Schubert and R. M. Hamwey, 1986: Large-amplitude

19   semidiurnal temperature variations in the polar mesopause: evidence of a

20   pseudotide. *Nature*, **324**(6095), 347-349.

21 Wang, L., M. A. Geller, and M. J. Alexander 2005: Spatial and temporal variations of gravity

22   wave parameters. Part I: Intrinsic frequency, wavelength, and vertical propagation

23   direction, *J. Clim.*, **62,** 125–142.

24 Watanabe, S., K. Sato, and M. Takahashi, 2006: A general circulation model study of the

25   orographic gravity waves over Antarctica excited by katabatic winds.

1   *J. Geophys. Res.,* **111**, D18104, doi:10.1029/2005JD006851.

2   Watanabe, S., K. Sato, Y, Kawatani, and M. Takahashi, 2015: Vertical resolution dependence

3   of gravity wave momentum flux simulated by an atmospheric general circulation

4   model, *Geosci. Model Dev.,* **8,** 1637-1644, doi:10.5194/gmd-8-1637-2015.

5   Wu, W.-S., R. J. Purser, and D. F. Parrish, 2002: Three-dimensional variational analysis with

6   spatially inhomogeneous covariances. *Mon. Wea. Rev.*, **130,** 2905–2916.

7   Wu, Q., Killeen, T. L., Nozawa, S., McEwen, D., Guo, W., & Solomon, S. C. (2003).

8   Observations of mesospheric neutral wind 12-hour wave in the Northern Polar

9   Cap. *Journal of atmospheric and solar-terrestrial physics*, **65**(8), 971-978.

10   Yamashita, K., S. Miyahara, Y. Miyoshi, K. Kawano, and J. Ninomiya, Seasonal variation of

11   non-migrating semidiurnal tide in the polar MLT region in a general circulation model,

12   *J. Atmos. Solar-Terr. Phys.*, **64**, 1083–1094, 2002.

13   Yasuda, Y., K. Sato, and N. Sugimoto, 2015: A Theoretical Study on the Spontaneous

14   Radiation of Inertia-gravity Waves Using the Renormalization Group Method. Part I:

15   Derivation of the Renormalization Group Equations,

16   *J. Atmos. Sci.*, **72**, 957–983, doi:10.1175/JAS-D-13-0370.1

17   Yasuda, Y., K. Sato, and N. Sugimoto, 2015: A Theoretical Study on the Spontaneous

18   Radiation of Inertia-gravity Waves Using the Renormalization Group Method. Part II:

19   Verification of the Theoretical Equations by Numerical Simulation,

20   *J. Atmos. Sci.*, **72**, 984–1009, doi:10.1175/JAS-D-13-0371.1

21   Yoshiki, M., and K. Sato (2000), A statistical study of gravity waves in the polar regions

22   based on operational radiosonde data, *J. Geophys. Res.*, **105**(D14), 17,995–18,011.

23   Zhang, F., S. E. Koch, C. A. Davis, and M. L. Kaplan, 2001: Wavelet analysis and the

24   governing dynamics of a large-amplitude mesoscale gravity-wave event along the East

25   Coast of the United States. *Quart. J. Roy. Meteor. Soc.,* **127,** 2209-2245.

1 **Table and Figure captions**

2 ● Table 1: The wave parameters of fluctuations in the mesosphere observed over Syowa

3 Station (a) obtained by fitting to a sinusoidal function using a nonlinear least square

4 method (b) estimated on the hypothesis that fluctuations are due to inertia-gravity waves,

5 where α is the angle of $u_\parallel$ measured clockwise from the east.

6 ● Table 2: The directly estimated wave parameters of packets simulated over Syowa

7 Station

8 ● Table 3: The results of the idealized ray tracing and the manual wave packet tracing

10 ● Figure 1:   (a) An illustration of the stretched grid (roughened up to glevel-3).   (b) A

11 horizontal map of a normalized grid interval defined as $d/\Delta x$, where d denotes grid

12 intervals and Δx denotes the grid interval of the original icosahedral grid.

13 ● Figure 2: Time-altitude cross sections of (a) eastward line of sight velocity components

14 observed by the PANSY radar at Syowa Station for the period from 17 March 2015 to 23

15 March 2015, (b) for the period from 21 March 2015 to 23 March 2015, and (c) opposite

16 of westward line of sight velocity components for the period from 21 March 2015 to 23

17 March 2015. The dashed line in (b) and (c) denotes phase lines with the downward phase

18 velocity of 0.3 m s^{-1}. The green arrows in (c) denotes the wave period of the disturbance.

19 The contour intervals are 2 m s^{-1}.

20 ● Figure 3: Time-altitude cross sections of (a) zonal wind components and (b) meridional

21 wind components observed by the PANSY radar at Syowa Station for the period from 17

22 March 2015 to 23 March 2015. The contour intervals are 12 m s^{-1}.

23 ● Figure 4: Zonal and meridional wind components observed on 23 March 2015 as a

24 function of time at heights of (a) 70.8 km and (b) 72.0 km. Zonal and meridional wind

25 components fitted sinusoidal functions using a nonlinear least squares method at the

1   height of (c) 70.8 km and (d) 72.0 km. The circles denote the zonal wind components and

2   the star marks denote the meridional components.

3   ● Figure 5: A hodograph of the fitted horizontal wind components in the time region from

4   00 UTC 23 to 13 UTC 23 March at the height of (a) 70.8 km and (b) 72.0 km from the

5   PANSY radar observation. Each mark is plotted at one hour interval.

6   ● Figure 6: Time-altitude cross sections of (a) eastward line-of-sight velocity components

7   simulated by NICAM at Syowa Station (contour interval 2 m s^{-1}) for the period from 17

8   March 2015 to 23 March 2015, (b) for the period from 21 March 2015 to 23 March 2015

9   (contour interval 3 m s^{-1}). (c) Zonal wind components in eastward line-of-sight velocity

10   components for the period from 21 March 2015 to 23 March 2015 (contour interval 18 m

11   s^{-1}).

12 ● Figure 7: Time-altitude cross sections of (a) anomalies of the zonal wind components

13   from the time-mean components, (b) the diurnal and semi-diurnal migrating tidal

14   components, (c) the planetary wave components, (d) small-scale gravity waves and (e)

15   the remaining components. The contour intervals are 10 m s^{-1}.

16 ● Figure 8: Time-altitude cross sections of the envelope function of the zonal wind

17   components of the large-scale gravity waves (contour interval 10 m s^{-1}) .The figure from

18   (i) to (v) denote the labels of the wave packet examined in Section 4.

19 ● Figure 9: A hovmoller diagram of zonal wind components of the large-scale inertia-

20   gravity waves at the height of 70 km at 69°S (contour interval 10 m s^{-1}). The figures (i),

21   (ii) and (v) indicate the packets labeled in Fig.5.

22 ● Figure 10: A composite map of zonal wind components of the large-scale inertia-gravity

23   waves. The height where the composites are taken and the reference time is (a) 70 km, 06

24   UTC 19 March, (b) 70 km, 15 UTC 20 March, (c) 75 km, 15 UTC 21 March, (d) 65 km,

25   03 UTC 22 March and (e) 72 km,14 UTC 22 March. The contour intervals are 10 m s^{-1}.

1. ● Figure 11: Snapshots of the zonal wind components and their envelope function of the
2. large-scale inertia-gravity waves (a) at the height of 70 km at 03 UTC 23 March 2015,
3. corresponding to the packet (v), and (c) at the height of 70 km at 01 UTC 19 March
4. 2015, corresponding to the packet (i). Hovmöller diagrams of the zonal wind components
5. and their envelope function of the large-scale inertia-gravity waves at the height of 70 km
6. at 69°S for the period (b) from 20 to 23 March and (d) from 17 to 20 March. The green
7. dashed curves in (a) and (c) denote the cross section taken in (b) and (d), and vice versa.
8. The green circles are locations of traced wave packets by the method discussed in the
9. text. The contour intervals are 10 m s⁻¹.
10. ● Figure 12: Snapshots of the zonal wind components of the large-scale inertia-gravity
11. waves tracing the packet (v) (a) at the height of 60 km at 23 UTC 22 March (contour
12. interval 10 m s⁻¹), (b) at the height of 40 km at 08 UTC 22 March (contour interval 5 m
13. s⁻¹), (c) at the height of 25 km at 16 UTC 21 March (contour interval 3 m s⁻¹) and (d) at
14. the height of 23 km at 03 UTC 21 March (contour interval 2 m s⁻¹). Snapshots for the
15. packet (i) (e) at the height of 63 km at 23 UTC 22 March, (f) at the height of 58 km at 15
16. UTC 18 March, (g) at the height of 53 km at 11 UTC 18 March (contour interval 5 m s⁻
17. ¹), (d) at the height of 48 km at 08 UTC 18 March (contour interval 3 m s⁻¹). The green
18. circles are locations of traced wave packets by the method discussed in the text.
19. ● Figure 13: The ray path of (a, b) the packet (v) and (c, d) the packet (i) using the
20. idealized ray tracing method (black thick line, colored circles) and the manual wave
21. packet tracing method (colored star marks) in (a, c) the latitude-height cross section and
22. (b, d) the horizontal map. The contours in (a, c) denotes background zonal wind
23. components averaged in the zonal direction and for the period from 17 March to 23
24. March.

1 ● Figure 14: A snapshots of longitude-height cross sections of zonal wind components of

2 the large-scale inertia-gravity waves (above the height of 19 km, the left color bar,

3 contour interval 2 m s^{-1}) and the absolute values of the horizontal wind components

4 (below the height of 18 km, the right color bar, contour interval 10 m s^{-1}) at 03 UTC 21

5 March at 40°S.

6 ● Figure 15: Snapshots of horizontal maps of (a) the absolute horizontal wind velocity and

7 (b) the residual of the nonlinear balance equation (ΔNBE) at the height of 10 km at 03

8 UTC 21 March 2015. The vectors in (a) denote the directions and the magnitude of the

9 horizontal winds. The contour intervals in (a) are 10 m s^{-1}.

10 ● Figure 16: (a) A longitude-height cross section of zonal wind components of the large-

11 scale inertia-gravity waves $\sqrt{\rho_0}u'$ at 69°S at 15 UTC 18 March (contour interval 0.1

12 Pa$^{0.5}$), and (b) a line plot of the energy flux $\overline{p'w'}$ averaged from the longitude of -90°E to

13 the longitude of 60°E. The thick black contours show background zonal wind components

14 extracted by a lowpass filter with a cutoff wavelength of 4000 km. The thick contours

15 denote 20 m s^{-1}, 30 m s^{-1} and 40 m s^{-1}, respectively.

16 ● Figure 17: Latitude-height cross sections of (a) the vertical fluxes of zonal momentum

17 $\rho_0\overline{u'w'}$, (b) the vertical fluxes of zonal momentum $\rho_0\overline{v'w'}$, (c) the ratio of the Coriolis

18 parameter to the intrinsic frequency $f/\hat{\omega}$, (d) the kinetic energies of the horizontal wind

19 components and (e) the potential energies of the large-scale inertia-gravity waves, which

20 are averaged in the zonal direction and for the period from 19 March to 21 March 2015.

21 The contour interval is (a, b) 2.0×10^{-5} [Pa], (c) 0.1, respectively. It should be noted

22 that the color bar and the contour interval in (d) and (e) are log-scaled.

Table 1:   The wave parameters of fluctuations in the mesosphere observed over Syowa Station (a) obtained by fitting to a sinusoidal function using a nonlinear least square method (b) estimated on the hypothesis that fluctuations are due to inertia-gravity waves, where α is the angle of $u_\parallel$ measured clockwise from the east.

Table 1a

Time and height locations	ω (s^{-1})	m (m^{-1}) from u'	C_{p_z}(m s^{-1}) from u'	m (m^{-1}) from v'	C_{p_z}(m s^{-1}) from v'
3/22 73.2 km	1.42×10^{-4} (12.3 h)				
3/22 73.8 km	1.27×10^{-4} (13.7 h)	5.24×10^{-4} (12.0 km)	-0.26	7.42×10^{-4} (8.47 km)	-0.19
3/22 74.4 km	1.59×10^{-4} (11.0 h)				
3/23 70.8 km	1.35×10^{-4} (12.9 h)				
3/23 71.4 km	1.35×10^{-4} (12.9 h)	4.08×10^{-4} (15.4 km)	-0.34	5.11×10^{-4} (12.3 km)	-0.28
3/23 72.0 km	1.42×10^{-4} (12.3 h)				

Table 1b

Time and height locations	$\lvert k_h \rvert$ (m^{-1})	k (m^{-1})	l (m^{-1})	α (degree)	$\dfrac{f}{\hat{\omega}}$
3/22 73.2 km	3.54×10^{-6} (1775 km)	$\pm 3.45 \times 10^{-6}$ (1821 km)	$\pm 0.79 \times 10^{-6}$ (7983 km)	12º	0.72
3/22 73.8 km	1.94×10^{-6} (3238 km)	$\pm 1.84 \times 10^{-6}$ (3414 km)	$\pm 0.62 \times 10^{-6}$ (10255 km)	18º	0.86
3/22 74.4 km	3.51×10^{-6} (1790 km)	$\pm 2.33 \times 10^{-6}$ (2699 km)	$\pm 2.63 \times 10^{-6}$ (2392 km)	48º	0.76
3/23 70.8 km	3.52×10^{-6} (1785 km)	$\pm 3.52 \times 10^{-6}$ (1783 km)	~ 0	2º	0.56
3/23 71.4 km	4.32×10^{-6} (1454 km)	$\pm 3.86 \times 10^{-6}$ (1626 km)	$\pm 1.95 \times 10^{-6}$ (3226 km)	14º	0.63
3/23 72.0 km	5.46×10^{-6} (1150 km)	$\pm 5.29 \times 10^{-6}$ (1188 km)	$\pm 1.35 \times 10^{-6}$ (4647 km)	14º	0.70

Table 2: The directly estimated wave parameters of simulated packets

Wave packets	k (m^{-1})	l (m^{-1})	m (m^{-1})	ω (s^{-1})	C_{p_x} (m s^{-1})	C_{p_z} (m s^{-1})	$\frac{f}{\widehat{\omega}}$
	$|k_h|$ (m^{-1})						
(i) z = 70 km 3/18 12 UTC ~ 3/19 24 UTC	-2.48×10^{-6} (2530 km)	~ 0	3.96×10^{-4} (15.8 km)	1.42×10^{-4} (12.3 h)	-57.3	-0.36	0.763
	2.48×10^{-6} (2530 km)						
(ii) z = 70 km 3/20 05 UTC ~ 3/21 01 UTC	-3.18×10^{-6} (1980 km)	-0.98×10^{-6} (6440 km)	4.10×10^{-4} (15.3 km)	1.47×10^{-4} (11.8 h)	-4.62	-0.36	0.704
	3.33×10^{-6} (1887 km)						
(iii) z = 75 km 3/21 03UTC ~ 3/22 03 UTC	-2.79×10^{-6} (2250 km)	-2.48×10^{-6} (2530 km)	3.92×10^{-4} (16.0 km)	1.99×10^{-4} (8.8 h)	-71.3	-0.51	0.617
	3.73×10^{-6} (1685 km)						
(iv) z = 65 km 3/21 21UTC ~ 3/22 09 UTC	-3.35×10^{-6} (1880 km)	-2.78×10^{-6} (2530 km)	4.63×10^{-4} (13.57 km)	1.46×10^{-4} (11.9 h)	-43.5	-0.32	0.617
	4.35×10^{-6} (1444 km)						
(v) z = 72 km 3/22 02 UTC ~ 3/23 02 UTC	-3.78×10^{-6} (1660 km)	-0.82×10^{-6} (7660 km)	4.52×10^{-4} (13.9 km)	1.59×10^{-4} (11.0 h)	-42.1	-0.35	0.653
	3.87×10^{-6} (1625 km)						

Table 3: The results of the manual wave packet tracing and the ray tracing

		Manual wave packet tracing			Ray tracing		
		Longitude[ºE]	Latitude [ºS]	Altitude [km]	Longitude[ºE]	Latitude [ºS]	Altitude [km]
Packet (v)	3/23 03 UTC	40	67	70.0	40.0	67.0	70.0
	3/22 23 UTC	68	66	60.0	46.2	65.6	63.9
	3/22 16 UTC	75	62	50.0	58.0	62.0	46.8
	3/22 08 UTC	63	52	40.0	71.5	57.2	33.1
	3/22 03 UTC	84	53	30.0	80.8	55.4	27.0
	3/21 16 UTC	80	43	25.0	103.3	51.1	10.3
	3/21 03 UTC	95	41	23.0	-	-	-
Packet (i)	3/19 01 UTC	30	70	70.0	30.0	70.0	70.0
	3/18 19 UTC	32	67	63.0	39.7	68.5	63.1
	3/18 15 UTC	33	66	58.0	47.0	66.7	56.3
	3/18 11 UTC	30	62	53.0	53.5	63.7	49.7
	3/18 08 UTC	30	59	48.0	57.7	61.0	44.6
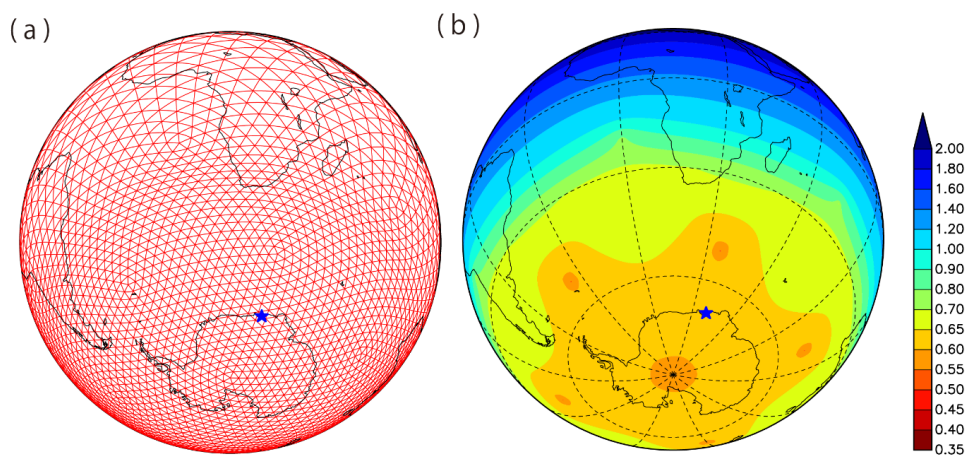
2   Figures

Figure 1:   (a) An illustration of the stretched grid (roughened up to glevel-3).   (b) A horizontal map of a normalized grid interval defined as $d/\Delta x$, where d denotes grid intervals and Δx denotes the grid interval of the original icosahedral grid.
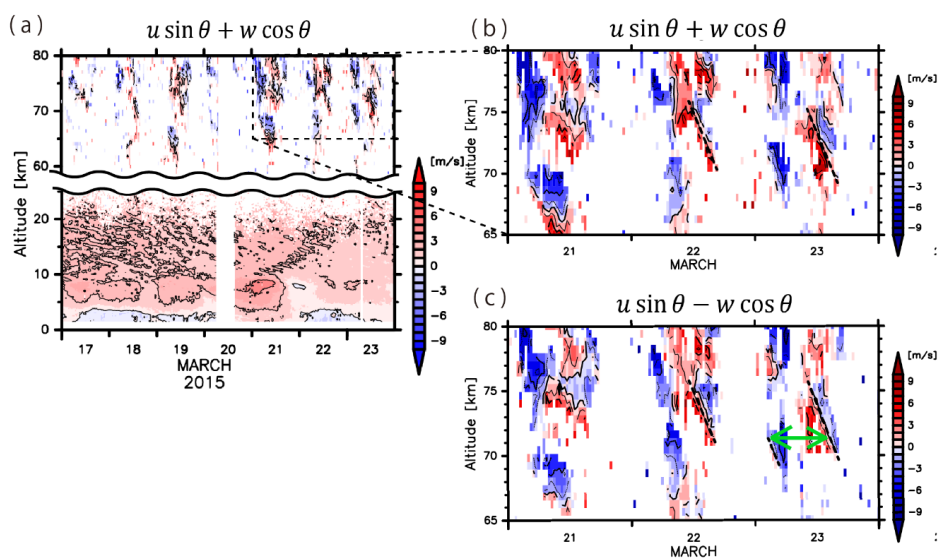
Figure 2: Time-altitude cross sections of (a) eastward line of sight velocity components observed by the PANSY radar at Syowa Station for the period from 17 March 2015 to 23 March 2015, (b) for the period from 21 March 2015 to 23 March 2015, and (c) opposite of westward line of sight velocity components for the period from 21 March 2015 to 23 March 2015. The dashed line in (b) and (c) denotes phase lines with the downward phase velocity of 0.3 m s^{-1}. The green arrows in (c) denotes the wave period of the disturbance. The contour intervals are 2 m s^{-1}.
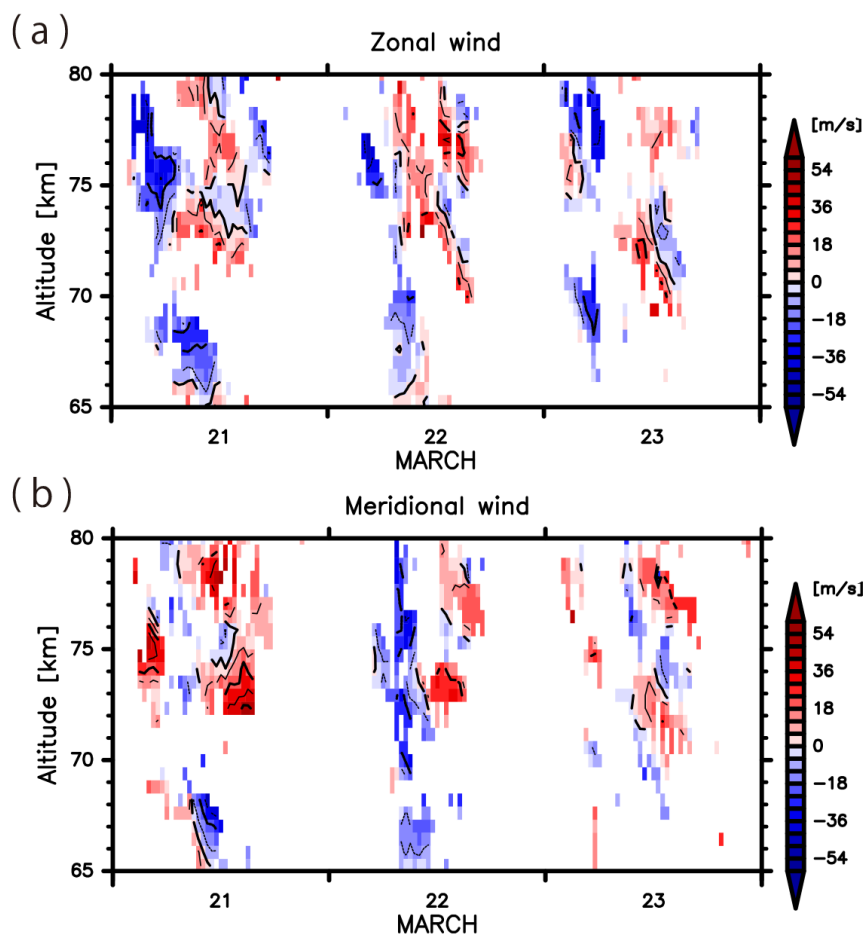
Figure 3: Time-altitude cross sections of (a) zonal wind components and (b) meridional

wind components observed by the PANSY radar at Syowa Station for the period from 17

March 2015 to 23 March 2015. The contour intervals are 12 m s^{-1}.
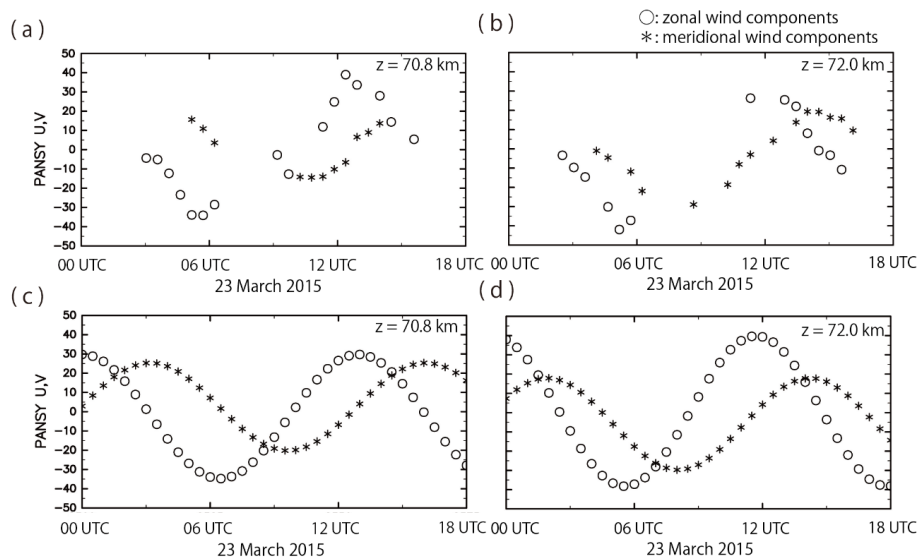
Figure 4: Zonal and meridional wind components observed on 23 March 2015 as a function of time at heights of (a) 70.8 km and (b) 72.0 km. Zonal and meridional wind components fitted sinusoidal functions using a nonlinear least squares method at the height of (c) 70.8 km and (d) 72.0 km. The circles denote the zonal wind components and the star marks denote the meridional components.
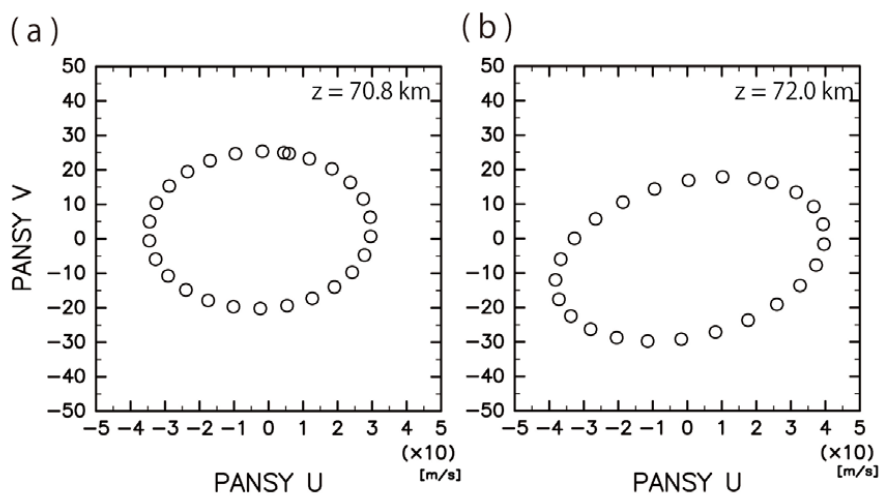
Figure 5 : A hodograph of the fitted horizontal wind components in the time region from 00

UTC 23 to 13 UTC 23 March at the height of (a) 70.8 km and (b) 72.0 km from the

PANSY radar observation. Each mark is plotted at one hour interval.
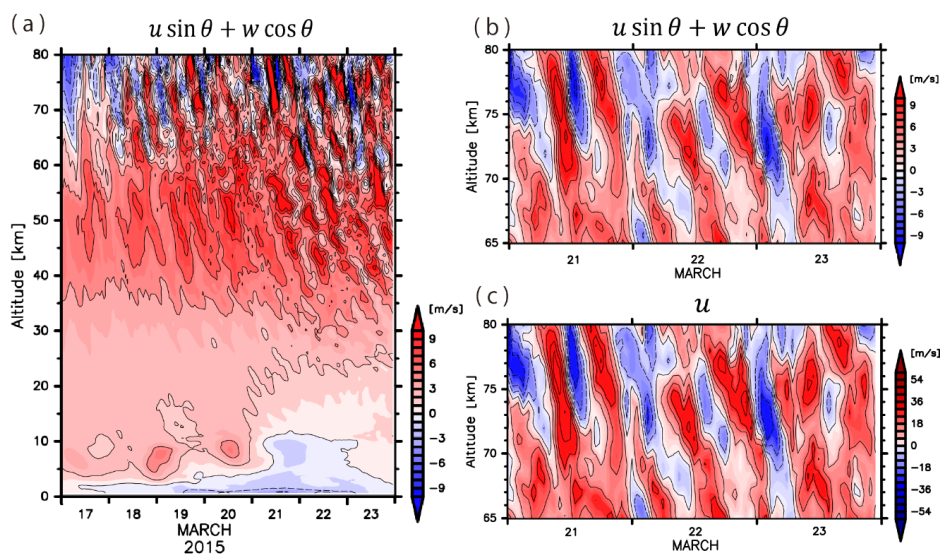
Figure 6: Time-altitude cross sections of (a) eastward line of sight velocity components simulated by NICAM at Syowa Station (contour interval 2 m s^{-1}) for the period from 17 March 2015 to 23 March 2015, (b) for the period from 21 March 2015 to 23 March 2015 (contour interval 3 m s^{-1}). (c) Zonal wind components in eastward line of sight velocity components for the period from 21 March 2015 to 23 March 2015 (contour interval 18 m s^{-1}).
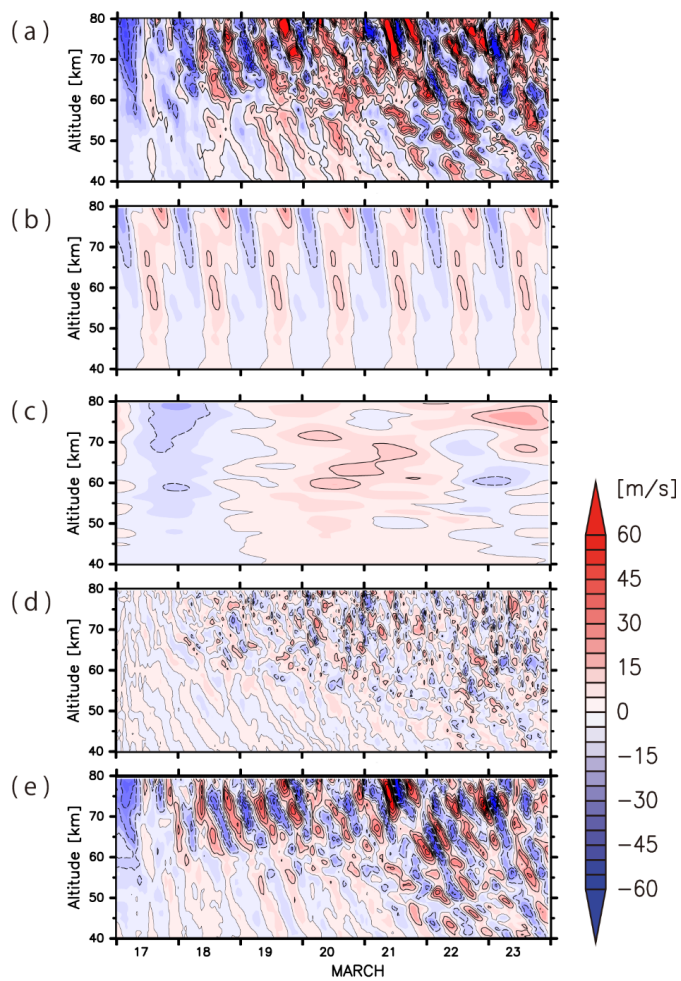
Figure 7: Time-altitude cross sections of (a) anomalies of the zonal wind components from

the time-mean components, (b) the diurnal and semi-diurnal migrating tidal components,

(c) the planetary wave components, (d) small-scale gravity waves and (e) the remaining

components. The contour intervals are 10 m s^{-1}.
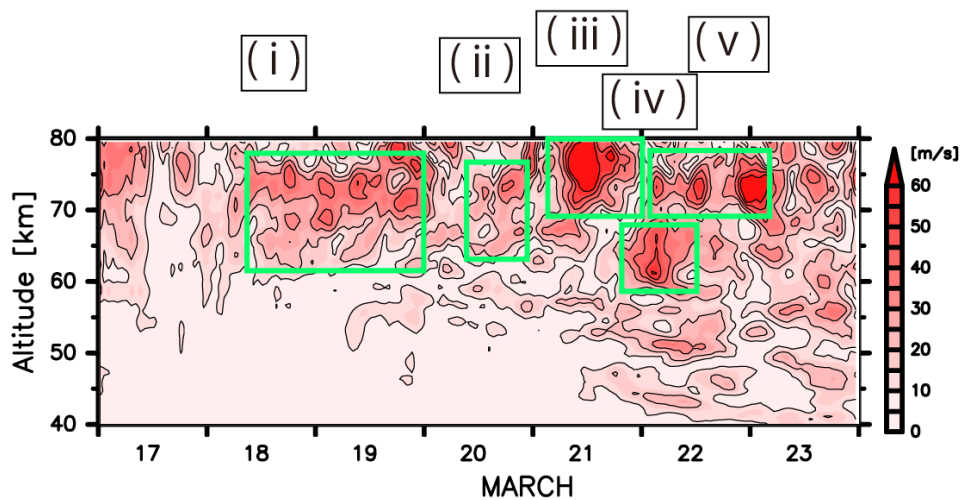
Figure 8: Time-altitude cross section of the envelope function of the zonal wind

components of the large-scale gravity waves (contour interval 10 m s^{-1}) .The figure from

(i) to (v) denote the labels of the wave packet examined in Section 4.
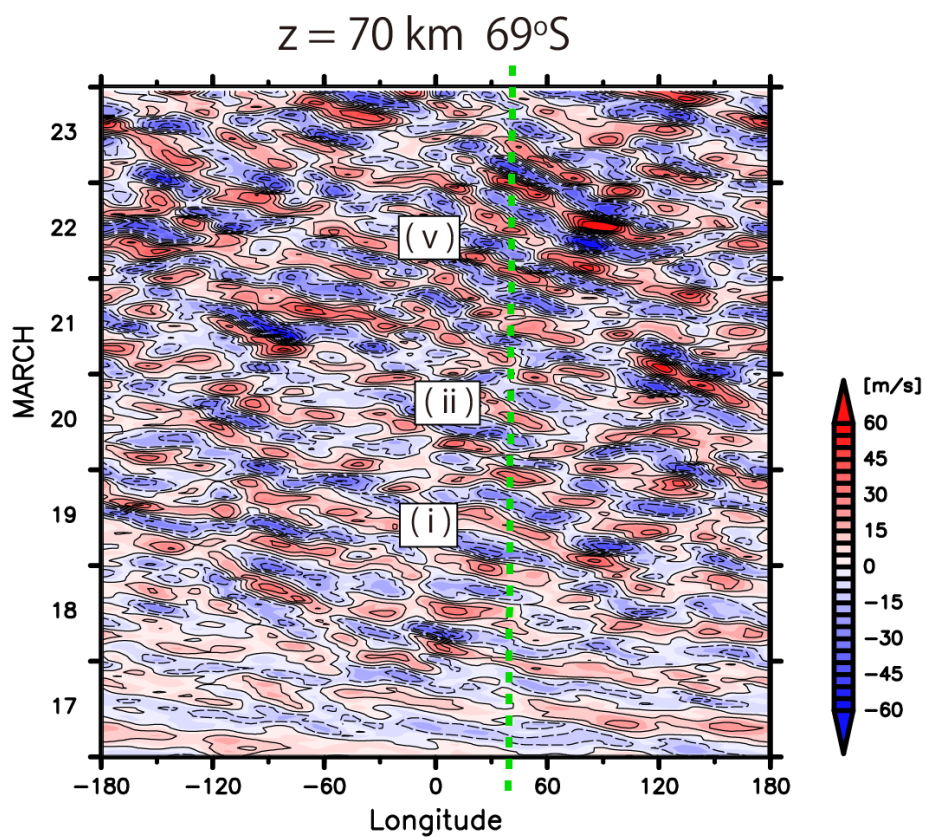
Figure 9: Hovmöller diagram of zonal wind components of the large-scale inertia-gravity waves at the height of 70 km at 69°S (contour interval 10 m s^{-1}). The figures (i), (ii) and (v) indicate the packets labeled in Fig.5.
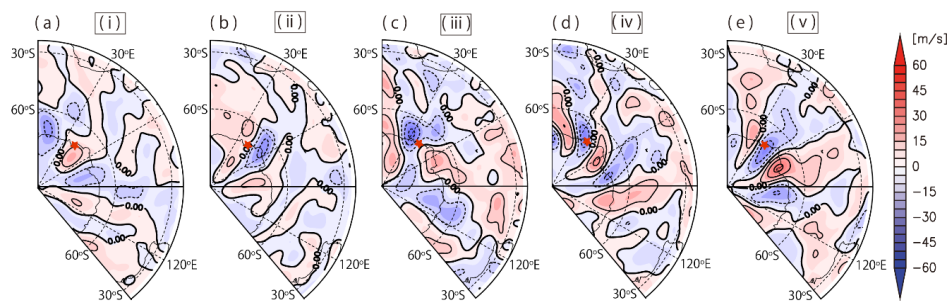
Figure 10: Composite maps of zonal wind components of the large-scale inertia-gravity waves. The height where the composites are taken and the reference time is (a) 70 km, 06 UTC 19 March, (b) 70 km, 15 UTC 20 March, (c) 75 km, 15 UTC 21 March, (d) 65 km, 03 UTC 22 March and (e) 72 km,14 UTC 22 March. The contour intervals are 10 m s^{-1}.
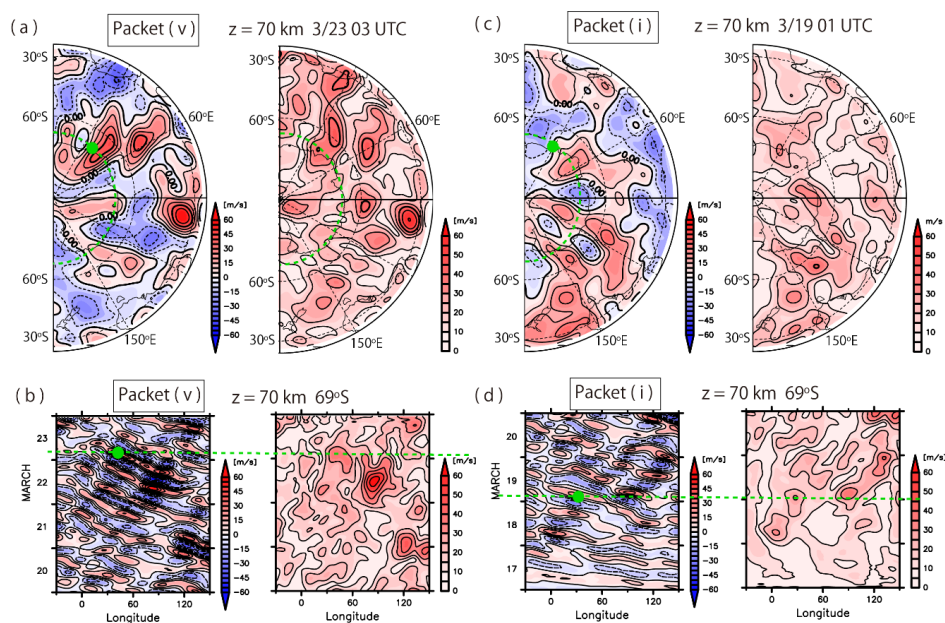
Figure 11: Snapshots of the zonal wind components and their envelope function of the large-scale inertia-gravity waves (a) at the height of 70 km at 03 UTC 23 March 2015, corresponding to the packet (v), and (c) at the height of 70 km at 01 UTC 19 March 2015, corresponding to the packet (i). Hovmöller diagrams of the zonal wind components and their envelope function of the large-scale inertia-gravity waves at the height of 70 km at 69°S for the period (b) from 20 to 23 March and (d) from 17 to 20 March. The green dashed curves in (a) and (c) denote the cross section taken in (b) and (d), and vice versa. The green circles are locations of traced wave packets determined by the method discussed in the text. The contour intervals are 10 m s^{-1}.
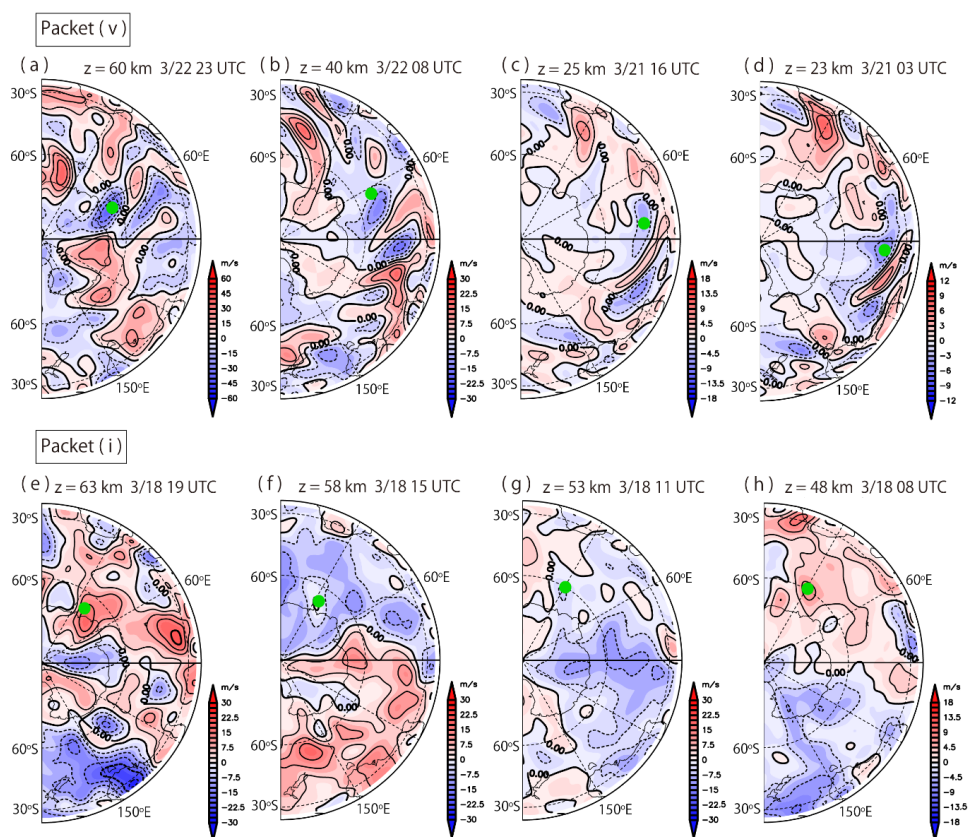
Figure 12: Snapshots of the zonal wind components of the large-scale inertia-gravity waves

tracing the packet (v) (a) at the height of 60 km at 23 UTC 22 March (contour interval 10

m s^{-1}), (b) at the height of 40 km at 08 UTC 22 March (contour interval 5 m s^{-1}), (c) at the

height of 25 km at 16 UTC 21 March (contour interval 3 m s^{-1}) and (d) at the height of 23

km at 03 UTC 21 March (contour interval 2 m s^{-1}). Snapshots for the packet (i) (e) at the

height of 63 km at 23 UTC 22 March, (f) at the height of 58 km at 15 UTC 18 March, (g)

at the height of 53 km at 11 UTC 18 March (contour interval 5 m s^{-1}), (d) at the height of

48 km at 08 UTC 18 March (contour interval 3 m s^{-1}).The green circles are locations of

traced wave packets determined by the method discussed in the text.
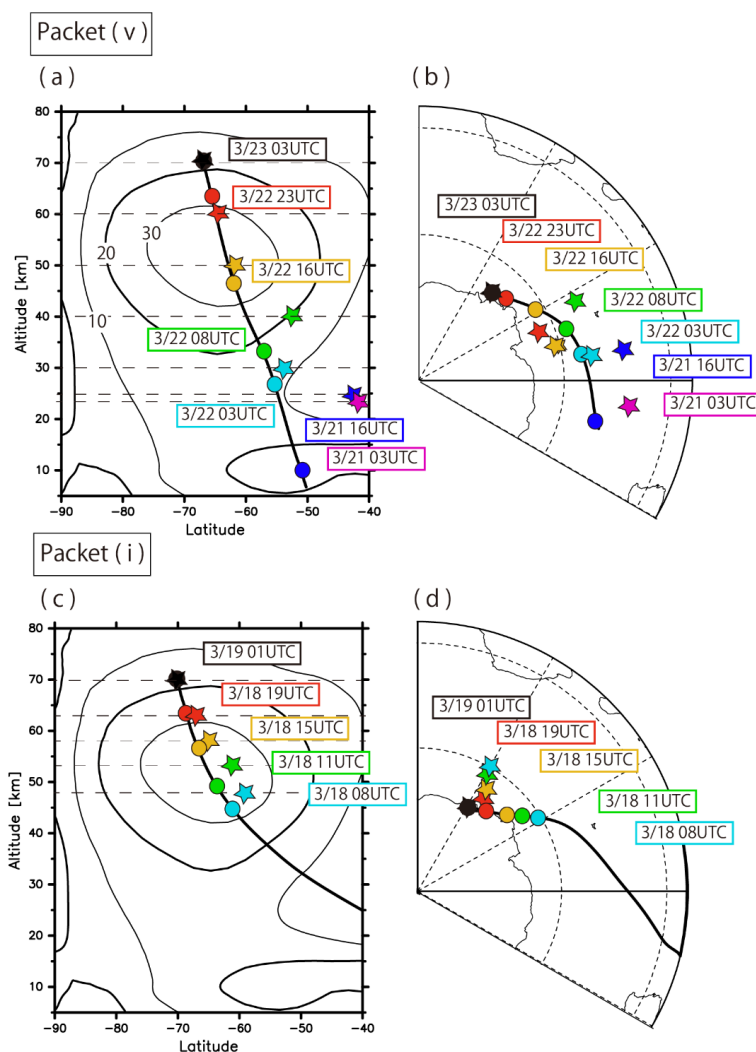
Figure 13: The ray path of (a, b) the packet (v) and (c, d) the packet (i) using the idealized

ray tracing method (black thick line, colored circles) and the manual wave packet tracing

method (colored star marks) in (a, c) the latitude-height cross section and (b, d) the

horizontal map. The contours in (a, c) denotes background zonal wind components

averaged in the zonal direction and for the period from 17 March to 23 March.
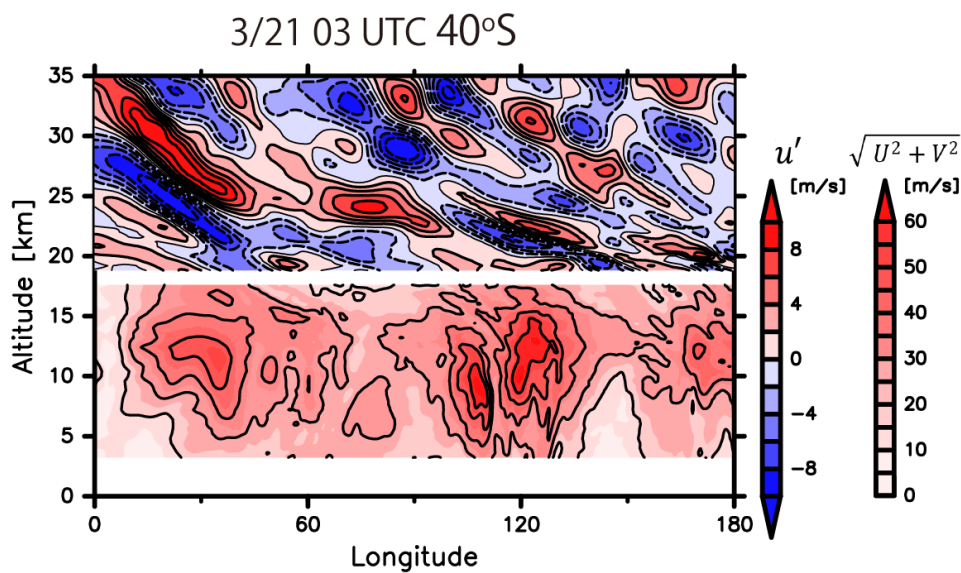
Figure 14: A snapshots of longitude-height cross sections of zonal wind components of the large-scale inertia-gravity waves (above the height of 19 km, the left color bar, contour interval 2 m s^{-1}) and the absolute values of the horizontal wind components (below the height of 18 km, the right color bar, contour interval 10 m s^{-1}) at 03 UTC 21 March at 40°S.
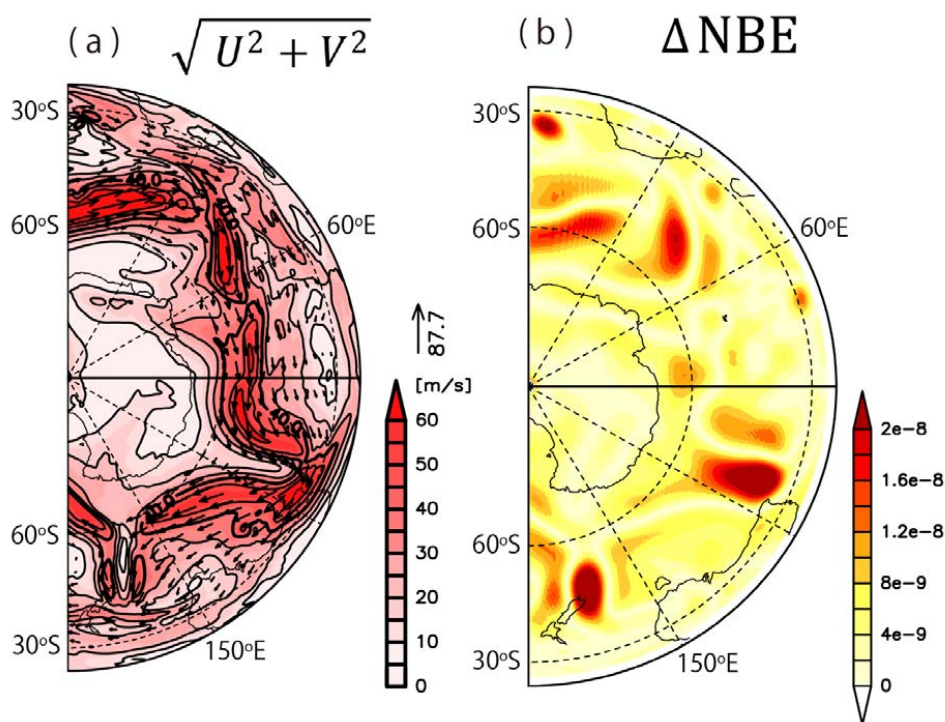
Figure 15: Snapshots of horizontal maps of (a) the absolute horizontal wind velocity and (b) the residual of the nonlinear balance equation (ΔNBE) at the height of 10 km at 03 UTC 21 March 2015. The vectors in (a) denote the directions and the magnitude of the horizontal winds. The contour intervals in (a) are 10 m s^{-1}.
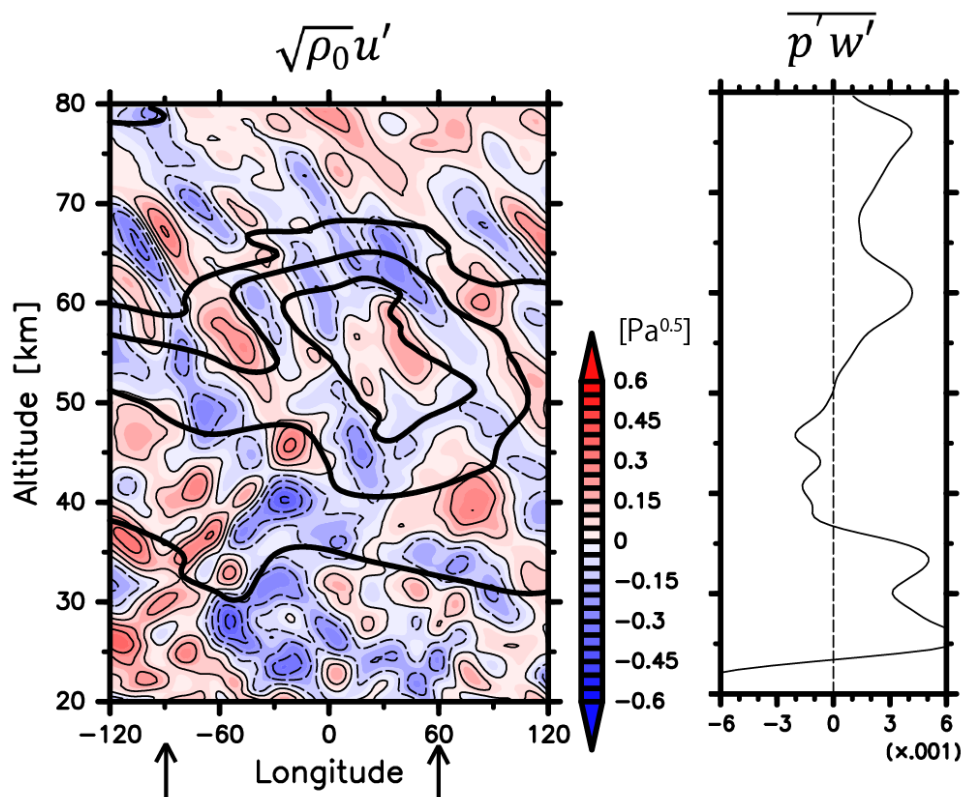
Figure 16: (a) A longitude-height cross section of zonal wind components of the large-scale inertia-gravity waves $\sqrt{\rho_0}u'$ at 69°S at 15 UTC 18 March (contour interval 0.1 Pa$^{0.5}$), and (b) a line plot of the energy flux $\overline{p'w'}$ averaged from the longitude of -90°E to the longitude of 60°E denoted by black arrows. The thick black contours show background zonal wind components extracted by a lowpass filter with a cutoff wavelength of 4000 km. The thick contours denote 20 m s^{-1}, 30 m s^{-1} and 40 m s^{-1}, respectively.
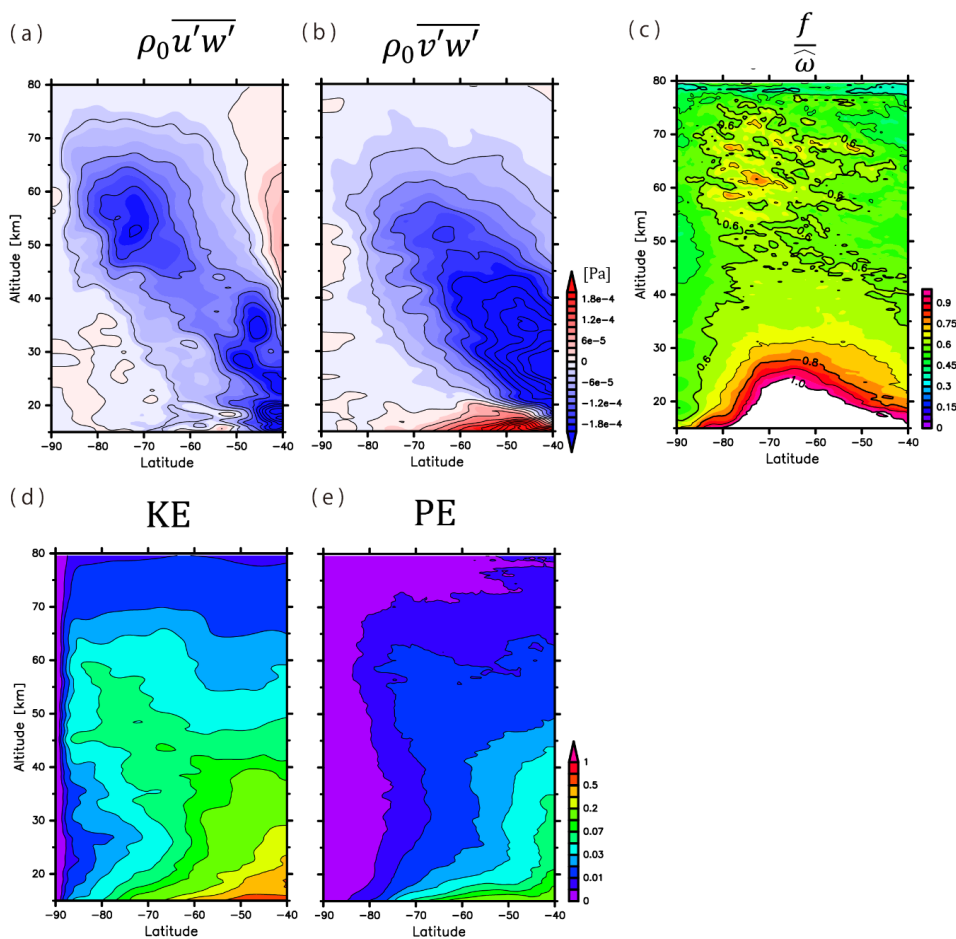
Figure 17: Latitude-height cross sections of (a) the vertical fluxes of zonal momentum $\rho_0\overline{u'w'}$, (b) the vertical fluxes of zonal momentum $\rho_0\overline{v'w'}$, (c) the ratio of the Coriolis parameter to the intrinsic frequency $f/\hat{\omega}$, (d) the kinetic energies of the horizontal wind components and (e) the potential energies of the large-scale inertia-gravity waves, which are averaged in the zonal direction and for the period from 19 March to 21 March 2015. The contour interval is (a, b) 4.0×10^{-5} [Pa] and (c) 0.1, respectively. It should be noted that the color bar and the contour interval in (d) and (e) are log-scaled.